AGU PUBLICATIONS

Global Biogeochemical Cycles

RESEARCH ARTICLE
10.1002/2017GB005630

Key Points:
- ENSO drives significant variability in tropical Pacific air-sea O_2 exchange
- The O_2 flux response to ENSO is driven primarily by ocean dynamics
- Atmospheric transport acts to amplify ENSO-related anomalies in atmospheric O_2

Correspondence to:
Y. A. Eddebbar,
yeddebba@ucsd.edu

Citation:
Eddebbar, Y. A., M. C. Long, L. Resplandy, C. Rödenbeck, K. B. Rodgers, M. Manizza, and R. F. Keeling (2017), Impacts of ENSO on air-sea oxygen exchange: Observations and mechanisms, *Global Biogeochem. Cycles*, *31*, 901–921, doi:10.1002/2017GB005630.

Received 27 JAN 2017
Accepted 9 MAY 2017
Accepted article online 11 MAY 2017
Published online 30 MAY 2017

Impacts of ENSO on air-sea oxygen exchange: Observations and mechanisms

Yassir A. Eddebbar[1], Matthew C. Long[2], Laure Resplandy[3], Christian Rödenbeck[4], Keith B. Rodgers[3], Manfredi Manizza[1], and Ralph F. Keeling[1]

[1]Scripps Institution of Oceanography, University of California, San Diego, California, USA, [2]National Center for Atmospheric Research, Boulder, Colorado, USA, [3]Program in Atmospheric and Oceanic Sciences, Princeton University, Princeton, New Jersey, USA, [4]Max Planck Institute for Biogeochemistry, Jena, Germany

Abstract Models and observations of atmospheric potential oxygen (APO $\simeq O_2 + 1.1 * CO_2$) are used to investigate the influence of El Niño–Southern Oscillation (ENSO) on air-sea O_2 exchange. An atmospheric transport inversion of APO data from the Scripps flask network shows significant interannual variability in tropical APO fluxes that is positively correlated with the Niño3.4 index, indicating anomalous ocean outgassing of APO during El Niño. Hindcast simulations of the Community Earth System Model (CESM) and the Institut Pierre-Simon Laplace model show similar APO sensitivity to ENSO, differing from the Geophysical Fluid Dynamics Laboratory model, which shows an opposite APO response. In all models, O_2 accounts for most APO flux variations. Detailed analysis in CESM shows that the O_2 response is driven primarily by ENSO modulation of the source and rate of equatorial upwelling, which moderates the intensity of O_2 uptake due to vertical transport of low-O_2 waters. These upwelling changes dominate over counteracting effects of biological productivity and thermally driven O_2 exchange. During El Niño, shallower and weaker upwelling leads to anomalous O_2 outgassing, whereas deeper and intensified upwelling during La Niña drives enhanced O_2 uptake. This response is strongly localized along the central and eastern equatorial Pacific, leading to an equatorial zonal dipole in atmospheric anomalies of APO. This dipole is further intensified by ENSO-related changes in winds, reconciling apparently conflicting APO observations in the tropical Pacific. These findings suggest a substantial and complex response of the oceanic O_2 cycle to climate variability that is significantly (>50%) underestimated in magnitude by ocean models.

1. Introduction

Dissolved oxygen (O_2) is essential to life in the ocean. As anthropogenic warming reduces O_2 solubility and weakens the ventilation of the ocean's interior, oceanic O_2 content is expected to decline [*Sarmiento et al.*, 1998; *Bopp et al.*, 2002; *Keeling and Garcia*, 2002], with potentially serious and widespread implications for marine ecosystems, global fisheries, and biogeochemical cycles of carbon, nutrients, and nitrous oxide [*Keeling et al.*, 2010]. Several studies suggest this decline, i.e., "deoxygenation," is already underway [*Stramma et al.*, 2008; *Helm et al.*, 2011; *Andrews et al.*, 2013]. Regionally, however, the attribution of O_2 changes remains challenging due to natural climate variability, which drives substantial O_2 variations on interannual to multidecadal time scales, obscuring the detection of forced trends [*Emerson et al.*, 2004; *Frölicher et al.*, 2009; *Deutsch et al.*, 2011; *Rodgers et al.*, 2015; *Long et al.*, 2016]. Interannual variability in physical and biogeochemical processes and their interactions are especially important as their integrated effects can lead to pronounced decadal [O_2] variability [*Ito and Deutsch*, 2010, 2013]. Another challenge is that models show poor skill in simulating [O_2] distributions and change, particularly in the tropical Pacific, where models and observations disagree on both magnitude and sign of subsurface [O_2] change [*Stramma et al.*, 2012; *Bopp et al.*, 2013; *Cocco et al.*, 2013]. These discrepancies arise from deficiencies in model representation of the competing effects of biology, transport, and thermodynamic processes on [O_2] variability [*Cabré et al.*, 2015].

The natural variability of the oceanic oxygen cycle also has important implications for understanding the global carbon cycle. Atmospheric O_2 and CO_2 measurements have long been used to resolve global land and ocean carbon sinks [*Keeling et al.*, 1996]. This method is based on key differences in terrestrial versus oceanic O_2 and CO_2 exchanges with the atmosphere: land uptake of anthropogenic CO_2 is driven by photosynthesis that produces O_2, whereas ocean CO_2 uptake involves carbonate chemistry and no associated O_2

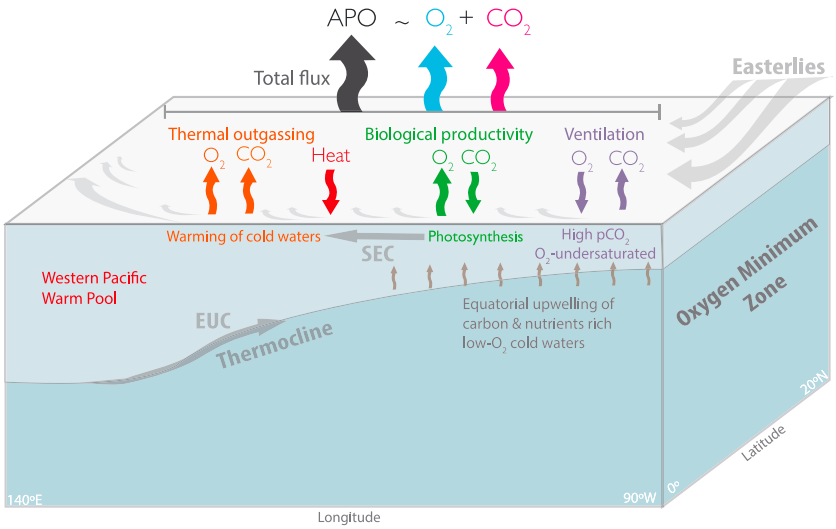

Figure 1. Schematic of major physical and biogeochemical processes driving the mean fluxes of O_2, CO_2, and atmospheric potential oxygen (APO) in the tropical Pacific. The Equatorial Undercurrent (EUC) and the South Equatorial Current (SEC) are also shown in dark grey arrows.

exchange [*Keeling et al.*, 1993]. A complication with this method is that air-sea O_2 flux can also vary due to natural variability-related processes that are not directly tied to the uptake of anthropogenic CO_2 [*Keeling et al.*, 1993; *Keeling and Garcia*, 2002; *McKinley et al.*, 2003; *Resplandy et al.*, 2014]. These additional fluxes must thus be accounted for to properly resolve the land and ocean carbon sinks [*Manning and Keeling*, 2006]. The magnitude and processes driving the natural variability of air-sea O_2 exchange, however, remain poorly understood, involving complex interactions between climate and ocean biogeochemical cycles.

In this study, we investigate the influence of El Niño–Southern Oscillation (ENSO), the leading mode of interannual climate variability, on the air-sea exchange of O_2. ENSO phenomena provide an ideal framework to (i) understand mechanisms driving the upper ocean O_2 cycle response to climate forcing on interannual to decadal time scales, (ii) constrain the role of natural variability in observed atmospheric and oceanic O_2 trends, and (iii) test models' representation of coupled climate-biogeochemical dynamics.

Figure 1 illustrates the major physical and biogeochemical processes driving air-sea fluxes of O_2 and CO_2 in the tropical Pacific. The prevailing easterlies drive Ekman upwelling of dissolved inorganic carbon (DIC)-rich and O_2-depleted waters in the eastern tropical Pacific and along the equator, causing strong outgassing of CO_2 and uptake of O_2 [*Wanninkhof et al.*, 1995; *Takahashi et al.*, 1997]. This upwelling of low-O_2 thermocline waters maintains an extensive equatorial band of O_2-undersaturated waters at the surface that extends through the central equatorial Pacific (Figure 2). These upwelled waters are also rich in nutrients, which fertilize the photosynthetic production of O_2 in the euphotic zone, thereby counteracting the O_2 deficit caused by upwelling, driving O_2 outgassing as these waters spread away from the equator [*Wanninkhof et al.*, 1995; *Najjar and Keeling*, 2000]. Concurrently, warming of these cold upwelled waters due to surface heating drives the outgassing of both CO_2 and O_2 due to the dependence of gas solubility on temperature [*Keeling et al.*, 1993]. The net balance of these dynamic, biological, and thermal processes in the tropical Pacific results in an intense natural source of both O_2 and CO_2 to the atmosphere [*Takahashi et al.*, 1997; *Gruber et al.*, 2001]. This large O_2 outgassing in the tropical Pacific is balanced globally by uptake at higher latitudes, where poleward transport of warm waters and seasonal vertical mixing induce substantial heat loss and ventilation of low-O_2 waters [*Najjar and Keeling*, 2000].

ENSO strongly modulates upper ocean dynamics and biogeochemistry in the tropical Pacific. At the onset of El Niño, westerly wind anomalies excite the eastward propagation of downwelling equatorial Kelvin waves that deepen the thermocline in the eastern equatorial Pacific [*McPhaden et al.*, 1998]. Ocean-atmosphere feedbacks reinforce the full development of El Niño [*Bjerknes*, 1969], as sea surface temperatures (SSTs)

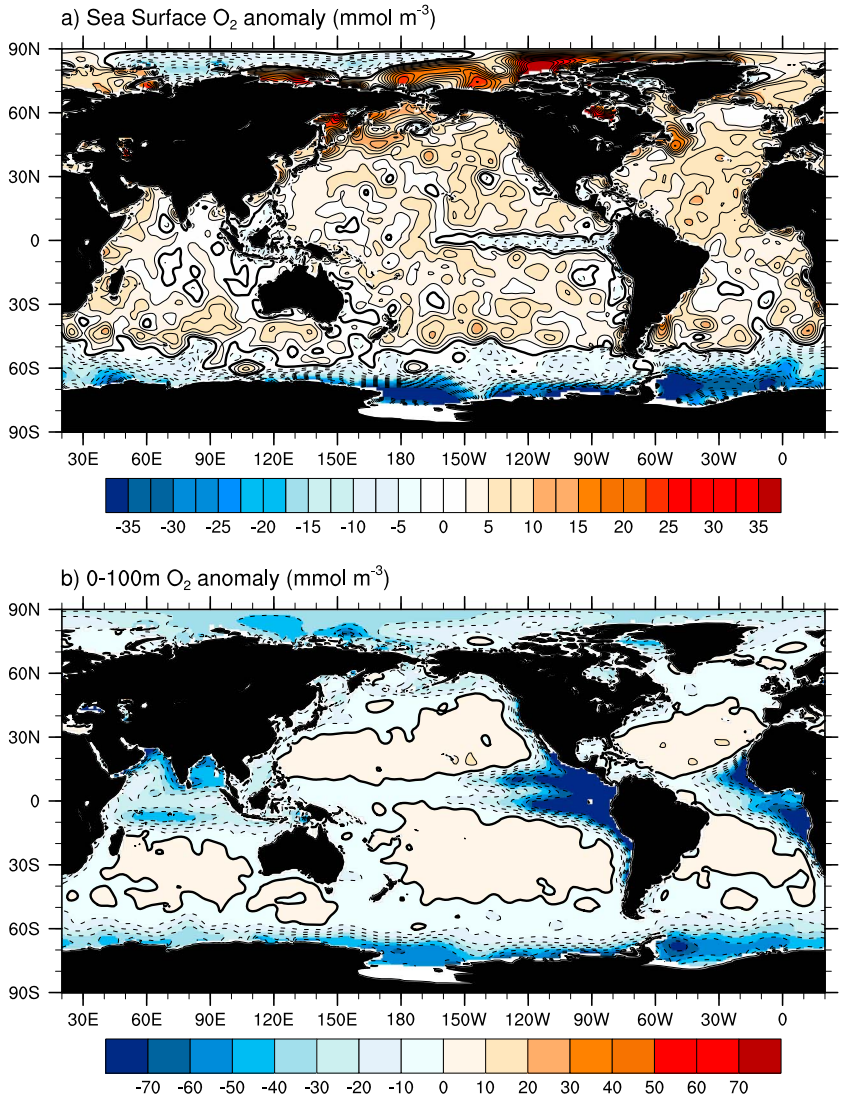

Figure 2. Annual mean climatology of O_2 anomaly ($\Delta O_2 = [O_2] - [O_2]_{sat}$) in mmol m^{-3} at (a) sea surface and (b) averaged over the upper 100 m of the ocean, calculated based on O_2, temperature, and salinity data from the World Ocean Atlas, 2013 [*Garcia et al.*, 2014] and the O_2 solubility equations of *Garcia and Gordon* [1992].

warm, the easterlies slacken, and upwelling weakens, driving significant biogeochemical changes. During the well-observed El Niño event of 1997–1998, for instance, upwelling of nutrients and DIC in the central equatorial Pacific appears to have ceased for several months, biological productivity was nearly halved, and surface pCO_2 reached values near equilibrium with the atmosphere, significantly weakening the typically strong natural outgassing of CO_2 in the tropical Pacific [*Chavez et al.*, 1999]. In the transition to La Niña conditions in mid-1998, strong upwelling resumed, biological productivity was enhanced, and CO_2 outgassing intensified [*Feely et al.*, 2002]. Whereas the influence of ENSO on the air-sea flux of CO_2 has been extensively studied for decades [*Bacastow*, 1976; *Keeling and Revelle*, 1985; *Winguth et al.*, 1994; *Chavez et al.*, 1999; *Feely et al.*, 1999, 2002; *McKinley et al.*, 2004; *Long et al.*, 2013], little is known about corresponding impacts on O_2 [*McKinley et al.*, 2003]. Detecting the net balance and contributions of the dynamic, biological, and thermal processes driving the air-sea O_2 flux response is difficult due to their competing effects and is further challenged by the lack of ocean biogeochemical observations that resolve the spatial and temporal extents of ENSO.

The imprints of ENSO on the air-sea exchange of O_2, however, are potentially detectable in time series of atmospheric O_2, measured as the $\delta(O_2/N_2)$ ratio and sampled by the Scripps Atmospheric Oxygen Program

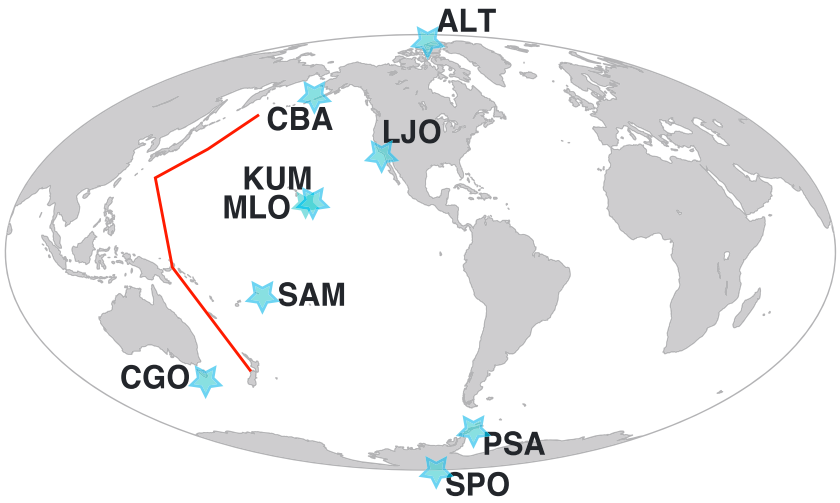

Figure 3. Location of Scripps APO sampling stations (blue stars) and shipboard measurement cruise lines (red line) used in *Tohjima et al.* [2015]. Stations are abbreviated and located as follows: Alert, Canada (ALT); Cold Bay, Alaska (CBA); La Jolla, CA (LJO); Mauna Loa Observatory, HI (MLO); Kumakahi, HI (KUM); Samoa Island, USA (SAM); Cape Grim, Australia (CGO); Palmer Station, Antarctica (PSA); and South Pole Observatory, Antarctica, (SPO).

at stations throughout the Pacific basin (Figure 3). For instance, an increase of ocean O_2 uptake driven by cooling or ventilation of low-O_2 waters is reflected as a decrease in the atmospheric O_2 content. Terrestrial processes, however, also influence atmospheric O_2. To isolate variability due to air-sea fluxes, we use atmospheric potential oxygen (APO), a tracer of ocean biogeochemistry [*Stephens et al.*, 1998; *Gruber et al.*, 2001]. APO is calculated as follows:

$$\delta\mathrm{APO} = \delta(\mathrm{O_2/N_2}) + 1.1 \cdot \frac{[\mathrm{CO_2}]}{X_{\mathrm{O_2}}}, \tag{1}$$

where the sum of $\delta(O_2/N_2)$ and CO_2 using the 1.1 biospheric $-O_2$:CO_2 molar exchange ratio cancels out the coupled influence of terrestrial photosynthesis and respiration [*Severinghaus*, 1995], and X_{O2} (0.2095), the atmospheric mixing ratio of O_2, converts $[CO_2]$ from parts per million to the per meg unit used in $\delta(O_2/N_2)$ measurements. While fossil fuel combustion and oceanic uptake of anthropogenic carbon drive the observed long-term downward trend in APO [*Manning and Keeling*, 2006], their effects on the variability of APO on interannual time scales are negligible [*Hamme and Keeling*, 2008]. Interannual variability in APO thus represents mainly changes in response to the air-sea fluxes of O_2 and CO_2. Due to buffering by carbonate chemistry, the time scale for CO_2 equilibration is about 1 order of magnitude slower than for O_2 [*Williams and Follows*, 2011]; consequently, O_2 fluxes are likely to dominate APO variability on interannual time scales [*Keeling and Severinghaus*, 2000]. APO observations thus provide an integrated constraint on the interannual variability of the air-sea O_2 flux and its coupling to climate variability.

The APO response to ENSO, however, is not well understood. Using APO data from Scripps stations over the 1994–2007 period and a global atmospheric transport inversion (referred to herein as "atmospheric inversion"), *Rödenbeck et al.* [2008] found a moderate positive correlation between the multivariate ENSO index and tropical APO fluxes, suggesting that El Niño conditions drive anomalous outgassing of APO, likely associated with variations in the ventilation of the tropical Pacific oxygen minimum zone (OMZ). Recently, however, using shipboard measurements of APO along the western Pacific (red lines in Figure 3) over the 2002–2012 period, *Tohjima et al.* [2015] showed a reduction of APO in the tropical Pacific during El Niño and an increase during La Niña. Tohjima and colleagues attribute these anomalies mainly to the effects of ENSO-related variations in atmospheric transport on surface APO distributions, reinforced by small variations in air-sea fluxes of CO_2. While the findings of *Tohjima et al.* [2015] seem to contradict the inferred relation between the Scripps APO record and ENSO, they may simply reflect complex phenomena that are not resolved by the sparse tropical observations network or these studies' short analysis periods.

In this study, we focus on the following questions:

1. How do ocean models simulate the APO flux response to ENSO compared to observation-based estimates?
2. What drives the APO response to ENSO in ocean models? Specifically, what mechanisms govern the O_2 flux response to ENSO in the tropical Pacific?
3. What is the role of atmospheric transport in driving surface variability of APO due to ENSO?

We address these questions using a combination of observations and models. First, we examine the fingerprints of ENSO on APO fluxes estimated using the atmospheric inversion method extended thru December 2015 and compare this response to APO flux simulations from three ocean models. To explore mechanisms driving the O_2 response to ENSO, we focus on a hindcast simulation of the Community Earth System Model (CESM). Next, using an atmospheric transport model and APO fluxes from the CESM simulation, we evaluate the role of atmospheric transport and air-sea fluxes on surface APO anomalies due to ENSO. We conclude with a summary and a brief discussion on the oceanic O_2 cycle coupling to climate variability.

2. Methods

2.1. APO Observations and Atmospheric Inversion

We present inverse estimates of air-sea flux of APO based on data from flask samples collected by the Scripps O_2 Research Program (http://scrippso2.ucsd.edu/data) at a network of surface stations (Figure 3) over the January 1994 thru December 2015 period. At each station, free tropospheric air is sampled in glass flasks twice a month and analyzed for O_2 via the $\delta(O_2/N_2)$ ratio using interferometry and for CO_2 using an infrared analyzer at the Scripps Atmospheric Oxygen Program Laboratory [*Keeling and Manning*, 2014]. APO time series from Cold Bay, Alaska and Palmer Station, Antarctica are excluded due to their shorter observational periods, noting that their inclusion had no significant impact on the interannual trends in APO fluxes. We also exclude the Mauna Loa and the South Pole stations because their APO records prior to 1998 were somewhat compromised during flask sampling of (O_2/N_2) due to fractionation [*Manning*, 2001]. APO fluxes are estimated based on data from five Scripps stations (ALT, LJO, KUM, SAM, and CGO, shown in Figure 3) and a global atmospheric transport inversion using TM3, an atmospheric tracer transport model, as detailed in *Rödenbeck et al.* [2008].

To account for autocorrelation when calculating correlations between the APO flux from the atmospheric inversion and the Niño3.4 index, statistical significance is calculated using a nonparametric method based on creating a large number of synthetic time series ($>$100,000) with similar power spectra as the original APO time series but with randomized phases [*Ebisuzaki*, 1997]. Statistical significance and confidence intervals are expressed as p, the fraction of synthetic time series that show a larger magnitude of correlation with the Niño3.4 index than the original APO flux time series (i.e., $p = 0.05$ refers to the 95% confidence interval).

2.2. Ocean Model Simulations

To evaluate processes driving APO flux variability and more specifically the response of O_2 to ENSO, we focus on a hindcast simulation of the ocean and sea ice components of CESM version 1.0 [*Gent et al.*, 2011]. CESM simulates reasonably well ENSO dynamics [*Deser et al.*, 2012], the seasonal cycle of APO [*Nevison et al.*, 2015], and the oceanic carbon cycle response to climate variability [*Long et al.*, 2013]. Similarly to other coarse resolution models, CESM contains significant $[O_2]$ biases. The volume and spatial extents of OMZs in CESM, for instance, are overestimated, including the Indian and tropical Pacific OMZs [*Moore et al.*, 2013]. Nevertheless, CESM captures well the large-scale spatial pattern distribution of $[O_2]$ [*Long et al.*, 2016] and shows the closest match to observations in the tropical Pacific across models [*Cabré et al.*, 2015], providing a useful tool to assess mechanisms driving O_2 variability in the upper ocean.

The CESM ocean component is the Parallel Ocean Program 2 (POP2), a z-level hydrostatic primitive equation model with spherical coordinates, a uniform zonal resolution of 1.11°, and a meridional resolution that increases from 0.27° at the equator to 0.54° poleward of 33° [*Smith et al.*, 2010; *Danabasoglu et al.*, 2012]. The vertical grid has 60 levels with 10 m resolution in the upper 160 m, increasing to 250 m until 3500 m depth, then remaining constant at 250 m until bottom. The model uses the *Gent and McWilliams* [1990] parameterization for mesoscale eddy transport and an eddy-induced advection coefficient that varies in time and

space [*Danabasoglu and Marshall*, 2007]. The K-profile parameterization of *Large et al.* [1994] is used to model boundary layer dynamics with a latitude-dependent background internal wave diffusivity [*Danabasoglu et al.*, 2012]. Sea ice is simulated using the Community Ice Code version 4, which operates on the same grid as POP2 [*Hunke and Lipscomb*, 2008]. Ocean biogeochemistry is represented using the biogeochemical elemental cycle (BEC) model [*Moore et al.*, 2004, 2013]. BEC simulates lower trophic-level marine ecosystem dynamics using the nutrient-phytoplankton-zooplankton-detritus paradigm, including three phytoplankton functional groups controlled by light, temperature, and nutrients (N, P, Si, and Fe), one zooplankton type, and the CO_2 and O_2 cycles [*Moore et al.*, 2013; *Long et al.*, 2013].

In the CESM hindcast simulation, the ocean and sea ice components of CESM are forced under the Coordinated Ocean-Ice Reference Experiments (CORE-2 [*Griffies et al.*, 2009, 2012]) protocol, which includes interannually varying radiative and freshwater fluxes, as well as atmospheric state variables used to compute fluxes via bulk formulae [*Large and Yeager*, 2009]. Observed climatologies were used to initialize the biogeochemical fields, whereas initial conditions for ocean physics were based on outputs from a previous physics-only ocean-ice hindcast simulation [*Long et al.*, 2013]. Four 60 year cycles were run to spin up the model. During the spin up, biogeochemistry is simulated continuously, whereas physical fields are set back to their initial conditions at the start of every cycle to reduce model drift. After the fourth cycle, a transient simulation was run corresponding to the 1948–2008 "observed" period. To avoid the influence of discontinuities induced at the beginning of the 60 year transient simulation, we exclude the initial 12 years and thus limit our analysis to model outputs from January 1960 to December 2008.

In addition to CESM, APO fluxes from the atmospheric inversion and Scripps data are also compared to hindcast simulations of ocean components of the Institut Pierre-Simon Laplace (IPSL) model and the Geophysical Fluid Dynamics Laboratory (GFDL) model. The IPSL simulation employs the Nucleus for European Modeling of the Ocean model [*Madec*, 2008] coupled to the Pelagic Interactions Scheme for Carbon and Ecosystem Studies biogeochemical model [*Aumont et al.*, 2015]. The model has 46 vertical levels, a horizontal resolution that ranges between 0.2° and 0.5°, and is forced by the atmospheric fields from the DRAKKAR Forcing Set based on the ERA40 and ERA-Interim reanalysis over the 1920–2012 period [*Brodeau et al.*, 2009; *Bourgeois et al.*, 2016]. The GFDL simulation is based on the GFDL Modular Ocean Model version 5 model coupled to the Tracers of Ocean Phytoplankton and Allometric Zooplankton (TOPAZ) biogeochemical model version 2 [*Dunne et al.*, 2010]. GFDL-TOPAZ is forced similarly to CESM using the CORE-2 protocol [*Griffies et al.*, 2009, 2012] over the 1948–2007 period, following *Rodgers et al.* [2009]. The hindcast simulations of CESM, IPSL, and GFDL differ in their representation of atmospheric forcing, ocean circulation, and ocean biogeochemistry and thus provide a first-order estimate of the influence of model choice and atmospheric forcing on the simulated APO flux response to ENSO.

2.3. Air-Sea Flux Analysis

In all ocean models, the simulated air-sea fluxes of O_2 (F_{O2}) and CO_2 (F_{CO2}) are computed based on the air-sea gas exchange parameterization of *Wanninkhof* [1992], as

$$F_g = K_g(1 - f_{\mathrm{ice}})\left([g] - [g]_{\mathrm{sat}}\right), \tag{2}$$

where f_{ice} is the surface sea ice fraction, $[g]$ is the modeled surface gas concentration, and $[g]_{\mathrm{sat}}$ is the saturation gas concentration calculated based on surface temperature and salinity following *Garcia and Gordon* [1992] for O_2 and *Weiss* [1974] for CO_2. K_g represents the gas transfer coefficient, a function of wind speed and the temperature-dependent Schmidt numbers of O_2 and CO_2 [*Keeling et al.*, 1998; *Wanninkhof*, 1992]. Positive flux denotes sea-to-air flux or "outgassing," whereas negative flux describes air-to-sea flux or ocean "uptake."

We evaluate the contributions of F_{O2} and F_{CO2} to APO variability, by computing the air-sea flux of APO (F_{APO}), following *Rödenbeck et al.* [2008], as

$$F_{\mathrm{APO}} = F_{\mathrm{O_2}} + 1.1{\cdot}F_{\mathrm{CO_2}} - \frac{X_{\mathrm{O_2}}}{X_{\mathrm{N_2}}}F_{\mathrm{N_2}}, \tag{3}$$

where X_{O2} (0.2095) and X_{N2} (0.7815) represent the atmospheric mixing ratios of O_2 and N_2, respectively. F_{N2}, the air-sea flux of nitrogen (N_2), is driven mainly by temperature-induced changes in gas solubility and is computed offline at each ice-free surface grid point based on the heat flux scaling formula of *Keeling et al.* [1993]:

$$F_{N_2} = \frac{\partial N_2^{sol}}{\partial T} \cdot \frac{Q}{\rho \cdot C_p}, \quad (4)$$

where $\partial N_2{}^{sol}/\partial T$ is the derivative of N_2 solubility with respect to temperature, computed based on *Hamme and Emerson* [2004]. Q is the model net air-sea heat flux computed as the sum of short-wave, long-wave, latent, and sensible heat fluxes; ρ is the density of surface water; and C_P (3993 J kg^{-1} K^{-1}) is the specific heat capacity of seawater.

Air-sea O_2 exchange is driven by processes affecting the surface mixed layer O_2 inventory and saturation state. These include thermally driven O_2 fluxes, net community production of O_2, and the vertical transport of subsurface low-O_2 waters into the mixed layer, referred to here as "ventilation." Assuming instantaneous air-sea gas exchange, we estimate the contribution of these processes by decomposing F_{O2} into thermal (F_{THERM}), net community production (F_{NCP}), and ventilation (F_{VENT}) fluxes, following *Nevison et al.* [2015], as

$$F_{O_2} = F_{THERM} + F_{NCP} + F_{VENT}, \quad (5)$$

Similarly to F_{N2}, the thermal flux of O_2, F_{THERM}, is calculated as

$$F_{THERM} = \frac{\partial O_2^{sol}}{\partial T} \cdot \frac{Q}{\rho \cdot C_p}, \quad (6)$$

where $\partial O_2{}^{sol}/\partial T$ is the derivative of O_2 solubility with respect to temperature at sea surface, calculated following *Garcia and Gordon* [1992]. F_{NCP} represents the O_2 flux due to the net community production of O_2 in the mixed layer, which we approximate as

$$F_{NCP} = \int_{0m}^{100m} [\mathrm{prod}(O_2) - \mathrm{cons}(O_2)]dz, \quad (7)$$

where prod(O_2) and cons(O_2) represent the model source and sink terms of O_2 due to photosynthesis and respiration, integrated over the upper 100 m of the ocean. This depth is close to the annual mean mixed layer depth over most of the ocean, as well as the depth of net biological carbon uptake in CESM [*Jin et al.*, 2007; *Doney et al.*, 2009]. This estimate is also adequate for an upwelling zone, such as the equatorial Pacific, where waters down to 100 m are upwelled relatively quickly into the mixed layer. F_{VENT}, the air-sea flux of O_2 driven by ventilation, is calculated as a residual in equation (5) and represents mainly the component of the air-sea flux driven by upwelling or vertical mixing of O_2-depleted subsurface waters into the mixed layer. Note that upwelling of cold waters also leads to a thermal influx of O_2; changes in the temperature-dependent solubility of O_2 due to upwelling are thus implicitly accounted for in F_{THERM} as heat fluxes involve ocean dynamics.

As noted above, this decomposition method assumes that air-sea equilibration occurs instantly. Thus, the F_{VENT} residual term likely includes contributions from changes in gas exchange efficiency due to the dependence of the gas transfer velocity K_g on wind intensity, which is sensitive to ENSO. Analysis of model results indicates that the contribution of this effect to F_{O2} variability is an order of magnitude smaller than the contributions of O_2 saturation anomalies ($\Delta O_2 = [O_2] - [O_2]_{sat}$). F_{VENT} also likely includes small residuals that arise from the approximate nature of equations (6) and (7), which assume that the mixed layer equilibrates instantly in response to heat fluxes and biological production and neglects the effects of mixing and penetration of shortwave irradiance below the mixed layer on biological production and gas supersaturation [*Dietze and Oschlies*, 2005]. While disequilibrium in air-sea gas exchange was suggested to damp the magnitude (by ~20%) and induce a short lag (2 weeks) in the annual cycle of air-sea O_2 exchange [*Dietze and Oschlies*, 2005; *Jin et al.*, 2007], its contribution on interannual time scales has not been evaluated yet and a detailed analysis of these effects is outside the scope of this study.

To emphasize interannual variability, air-sea flux anomalies from the atmospheric inversion and the hindcast simulations for all models are calculated by removing the monthly mean seasonal cycle and a linear trend from all time series and smoothed using a Lanczos 18 month low-pass filter [*Duchon*, 1979]. The impacts of ENSO are quantified using a linear least squares regression of flux anomalies onto the standardized

Niño3.4 index, calculated following *Trenberth* [1997] for each hindcast simulation. Statistical significance is calculated using a *t* test, taking autocorrelation into account by adjusting the degree of freedom using the lag-one autocorrelation of the series [*Zwiers and von Storch*, 1995].

2.4. Atmospheric Transport Simulations

To evaluate the effects of changes in atmospheric transport on surface APO anomalies, we use the TM3 atmospheric transport model [*Heimann and Korner*, 2003]. Forward atmospheric simulations are performed using two different fluxes from the CESM hindcast simulation:

CLM_FLX transports the climatological annual cycle of F_{APO}, calculated as the long-term mean of linearly detrended F_{APO} at each month in CESM. This simulation isolates the effects of atmospheric transport variability on surface APO anomalies since the air-sea fluxes do not vary from year to year.

VAR_FLX transports the APO fluxes, as simulated by the CESM hindcast simulation where they vary from year to year. This atmospheric simulation thus includes the effects of variability in atmospheric transport as well as in air-sea fluxes.

These atmospheric transport simulations are carried out over the January 1970 to December 2008 period using 6-hourly wind fields from the updated National Centers for Environmental Prediction (NCEP) reanalysis [*Kalnay et al.*, 1996]. The seasonal cycle and long-term trends are removed from all transport simulations similarly to the air-sea flux analysis and smoothed using a 6 month low-pass filter to reduce noise associated with atmospheric synoptic events.

3. Results and Discussion

3.1. Comparison of Inversion Versus Ocean Simulations of F_{APO} Variability

Figure 4 shows the global and tropical air-sea flux of APO inferred from the atmospheric inversion and Scripps observations (F_{APO_INV}), compared to the CESM, IPSL, and GFDL "ocean" simulations (F_{APO_CESM}, F_{APO_IPSL}, and F_{APO_GFDL}). Note that F_{APO_INV} is scaled down by 50% in Figures 4a–4c and 4e–4g to allow for phase comparison with the ocean simulations. F_{APO_INV} shows significant variability globally ($1\sigma = \pm 84$ Tmol yr^{-1}) as well as in the tropics ($1\sigma = \pm 66$ Tmol yr^{-1}). The ocean simulations capture key features of this variability, including the peaks of 1997–1998, 2002–2003, and, for the extended IPSL simulation, the peak of 2009–2010. There are, however, notable disagreements between the atmospheric inversion and ocean simulations. These disagreements include a large negative anomaly during 2000–2001 and a positive anomaly during 2005 found in F_{APO_INV} but not in the ocean simulations. Across all ocean simulations, the magnitude of interannual variability in F_{APO} is significantly underestimated (>50%) globally and regionally when compared to F_{APO_INV} (Table 1). The underestimation of F_{APO} variability shown in these models is likely related to systemic model biases that we discuss in section 4.

The tropical region (20°N–20°S) plays a major role in driving anomalies in the global F_{APO_INV} (Figure 4d). We find a positive correlation between anomalies in tropical F_{APO} and the Niño3.4 index in the atmospheric inversion ($R_{APO\_inv} = 0.46$, 5 month F_{APO} lead, $p < 0.01$) as well as in the CESM and IPSL simulations ($R_{CESM} = 0.60$ at 5 month F_{APO} lead; $R_{IPSL} = 0.59$ at 4 month F_{APO} lead). This relation suggests that in both inversion and these ocean simulations, anomalous outgassing of APO in the tropics leads El Niño events, and conversely, anomalous drawdown of APO leads La Niña.

The atmospheric inversion shows an estimated APO flux response to ENSO of about 34 Tmol yr^{-1} σ^{-1} (σ here refers to one standard of deviation of the Niño3.4 index). Table 1 and Figures 5a and 5c show that both CESM and IPSL capture the sign and phase of this response to ENSO but underestimate its magnitude. GFDL, on the other hand, is in general disagreement in sign, magnitude, and phase with both the inversion and other ocean simulations (Figures 4e–4g and 5d), showing a negative lagged F_{APO} response to the Niño3.4 index ($R_{GFDL} = -0.67$, 7 month F_{APO} lag). While this negative response also exists in CESM and IPSL with different lags, these models show a positive APO anomaly leading the Niño3.4 index that is not simulated by GFDL (Figure 5d). The similar results shown in CESM and IPSL, which are forced differently (NCEP versus ERA-Interim), contrasted with GFDL, which is forced similarly to CESM, suggest that differences in model representation of ocean circulation and/or biogeochemistry, rather than atmospheric forcing, drive models divergence in the F_{APO} response to ENSO.

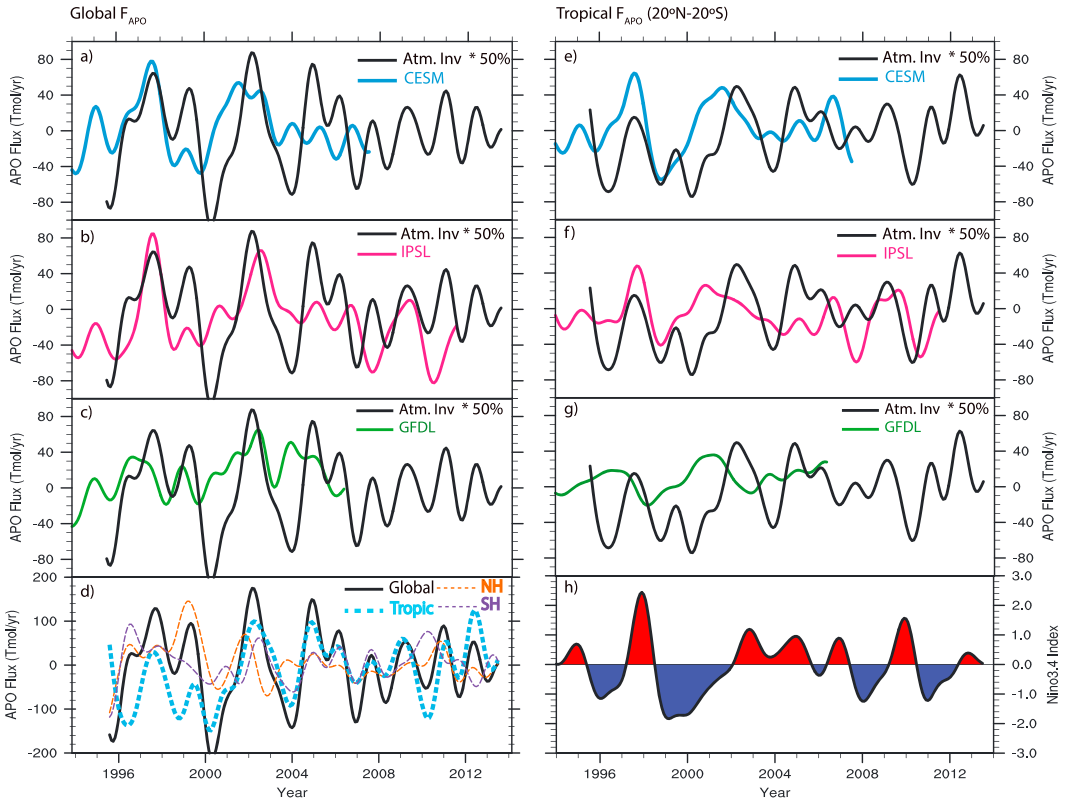

Figure 4. Comparison of global F_{APO} from the atmospheric inversion (black; scaled by 50%) versus (a) CESM, (b) IPSL, and (c) GFDL. (d) Regional contributions to F_{APO} inversion integrated over the tropics (blue, 20°N–20°S), northern extratropics (NH; orange, 20°N–90°N), and southern extratropics (SH, purple 20°S–90°S). (e–g) A similar comparison of F_{APO} as Figures 4a–4c but for the tropical region (20°N–20°S). Similarly to the global integral, the tropical F_{APO} estimate from the atmospheric inversion is scaled by 50% to allow for phase comparison to the ocean model simulations of F_{APO}. (h) Niño3.4 index over the comparison period (data obtained from NOAA website: http://www.cpc.ncep.noaa.gov). All time series are smoothed using an 18 month Lanczos low-pass filter. First and last 18 months of time series are omitted due to edge effects. Positive flux denotes sea-to-air flux or "outgassing."

3.2. Drivers of Tropical F_{APO} Variability

In all models, the tropical F_{APO} response to ENSO is driven primarily by F_{O2} (Figure 5). In CESM, for instance, the simulated F_{APO} response to ENSO of 21 Tmol APO yr^{-1} σ^{-1} is driven by anomalous outgassing of O_2 (28 Tmol yr^{-1} σ^{-1}) and is counteracted by a lagged anomalous uptake of CO_2 (−11 Tmol yr^{-1} σ^{-1}) damping the APO response (Figure 5a). F_{N2} also serves to damp F_{APO} variability, though its contribution to the total F_{APO} variability is very small compared to F_{O2} (Figure 6a). The dominance of F_{O2} on the interannual variability of F_{APO} is expected. Unlike CO_2, O_2 is not buffered by the ocean's inorganic carbonate chemistry, which allows O_2 a faster equilibration response time scale and a larger air-sea flux amplitude than CO_2, lending further confidence in using APO as a proxy for air-sea O_2 exchange on interannual time scales.

Table 1. Comparison of Global and Tropical F_{APO} Variability From the Atmospheric Inversion and Hindcast Model Simulations of CESM, IPSL, and GFDL

APO Flux Product	Analysis Period	1σ of Global F_{APO} (Tmol yr^{-1})	1σ of Tropical F_{APO} (Tmol yr^{-1})	Maximum Lag Correlation of Tropical F_{APO} Versus Niño3.4 Index	Tropical F_{APO} Response to Niño3.4 Index (Tmol yr^{-1} σ^{-1})
Atmospheric Inversion	1994–2015	±84.24	±66.23	0.46 (5 month F_{APO} lead)	33.88
CESM	1960–2008	±35.77	±29.87	0.62 (5 month F_{APO} lead)	20.79
IPSL	1960–2012	±40.40	±23.21	0.59 (4 month F_{APO} lead)	15.38
GFDL	1960–2007	±35.83	±19.28	−0.67 (7 month F_{APO} lag)	−14.44

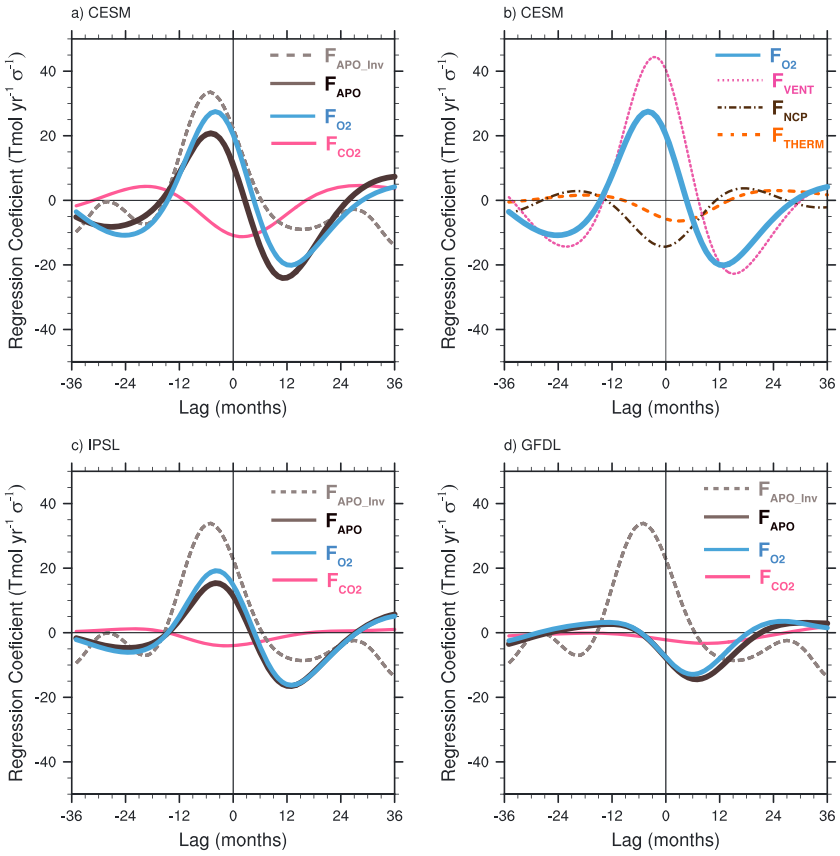

Figure 5. Lag regression of Niño3.4 index versus (a) tropical (20°N–20°S) F_{APO}, F_{O2}, and F_{CO2} in CESM and (b) tropical F_{O2} including flux components in CESM. (c and d) same as Figure 5a but for IPSL and GFDL. The atmospheric inverse F_{APO} is also shown (dashed grey) for comparison. All time series are smoothed using an 18 month low-pass filter prior to lag regression. Positive flux denotes sea-to-air flux or "outgassing."

Due to its central role in driving F_{APO} variability, we focus on the tropical F_{O2} response, which shows an even stronger positive correlation to the Niño3.4 index in CESM (R_{FO2} = 0.78, 4 month F_{O2} lead) compared to F_{APO} (R_{FAPO} = 0.62, 5 month lead; Table 1). The 4 month lead of the F_{O2} response likely reflects the sensitivity of surface ΔO_2 to changes in ocean dynamics, which lead the full development of El Niño events, typically defined by the mean SST anomaly of the Niño3.4 region [*Trenberth*, 1997]. This tight ENSO modulation of tropical F_{O2} variability reflects significant changes in the upper equatorial Pacific O_2 budget (upper 500 m of Pacific 5°N–5°S), whereby the upper ocean anomalously loses O_2 to the atmosphere during El Niño and, conversely, gains more O_2 during La Niña (Figures 6b and 6c).

The spatial pattern of the O_2 flux response to ENSO, as simulated in CESM, is illustrated in Figures 7a and 7b, which shows a regression of SST and F_{O2} anomalies onto the Niño3.4 index. The O_2 flux response to El Niño is marked by (i) significantly reduced O_2 uptake (i.e., strong anomalous outgassing) along the equatorial Pacific cold tongue and the upwelling regions of the eastern tropical Pacific and (ii) anomalous weak uptake west of 180° and poleward of the equator. Outside the tropics, weaker O_2 flux anomalies are also evident, with uptake in the North Pacific and outgassing in the Southern Ocean during El Niño. These anomalies are associated with changes in sea level pressure (SLP) and SST (Figure 7a) driven by ENSO teleconnections [*Trenberth et al.*, 2002; *Alexander et al.*, 2002]. Similar F_{O2} response patterns are simulated by IPSL and GFDL (Figures 7c and 7d), though regional contributions differ between models. IPSL, for instance, shows a less pronounced zonal gradient in the equatorial F_{O2} response than CESM and a weaker tropical F_{O2} response overall. GFDL, on the other hand, shows more confined outgassing along the eastern equatorial Pacific, counteracted by a significant opposing response outside the cold tongue, likely explaining its negative and weak integrated F_{APO} response to ENSO (Figure 5d).

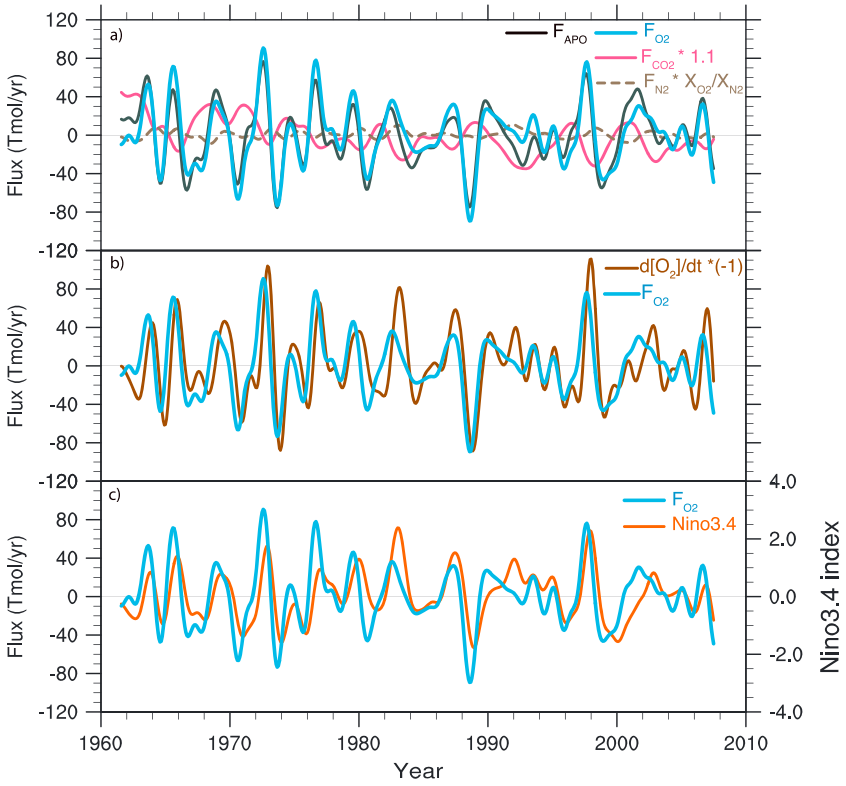

Figure 6. Time series from the CESM hindcast simulation of anomalies in (a) tropical F_{APO} (black), F_{O2} (blue), F_{CO2} (magenta), and F_{N2} (dashed grey), scaled by their contributions to F_{APO} following equation (3); (b) tropical F_{O2} (blue) versus volume integrated $d[O_2]/dt$ * (−1) over the upper 500 m of the upper equatorial Pacific (5°N–5°S; brown); and (c) tropical O_2 fluxes (blue) versus Niño 3.4 index (orange). All time series are smoothed using an 18 month low-pass filter. First and last 18 months of time series are omitted due to edge effects. Positive flux denotes sea-to-air flux or "outgassing."

3.3. Mechanisms of ENSO-Related Variability in Tropical F_{O2}

We now examine mechanisms driving the O_2 response to ENSO in CESM, focusing on the tropical Pacific region. ENSO-driven variability in tropical F_{O2} involves components that partly counteract each other (Figure 5b). F_{VENT}, the ventilation component of the O_2 flux, contributes an estimated ±44 Tmol yr^{-1} σ^{-1} (3 month F_{VENT} lead) to the net F_{O2} response, which is partly offset by F_{THERM}, the thermal component of O_2, and F_{NCP}, the net community production of O_2. Figures 8a–8d illustrate the spatial extent of these responses in the tropical Pacific, showing a significant reduction of the ventilation-driven uptake of O_2 along the equatorial cold tongue, which yields a larger flux impact than the concurrent weak reductions in biological production and thermal outgassing of O_2 during El Niño. Conversely, during La Niña, F_{VENT} is intensified significantly more than the counteracting increase in F_{NCP} and F_{THERM}. In the following, we elaborate on mechanisms driving the F_{O2} response during El Niño, noting that the reverse describes La Niña conditions.

Figure 8d shows the F_{VENT} response to El Niño as intense anomalous outgassing that extends broadly along the equator from the Peruvian upwelling system in the east to 160°E across the basin to the west. Figure 8h shows that this F_{VENT} anomaly is associated with significant changes in subsurface ΔO_2 changes (>10 mmol m^{-3} σ^{-1}) down to 400 m in depth. These equatorial ΔO_2 anomalies show a strong zonal dipole and maxima along the climatological equatorial oxycline (50–150 m in depth), driven by the vertical displacement of isopycnals as the thermocline deepens in the east and shoals in the west during El Niño. The lack of wind anomalies in the eastern tropical Pacific despite large anomalies in F_{VENT} (Figures 8d and 8e) and the 3 month lead of the F_{VENT} response suggest that the main physical driver affecting ΔO_2 and F_{VENT} in this region is remote forcing by the eastward propagation of equatorial Kelvin waves. Kelvin waves act to deepen the eastern equatorial Pacific thermocline [*McPhaden et al.*, 1998; *Feely et al.*, 2002], leading to shallower upwelling, reduced supply of O_2-depleted waters to the surface and weakened O_2 ingassing. On the other

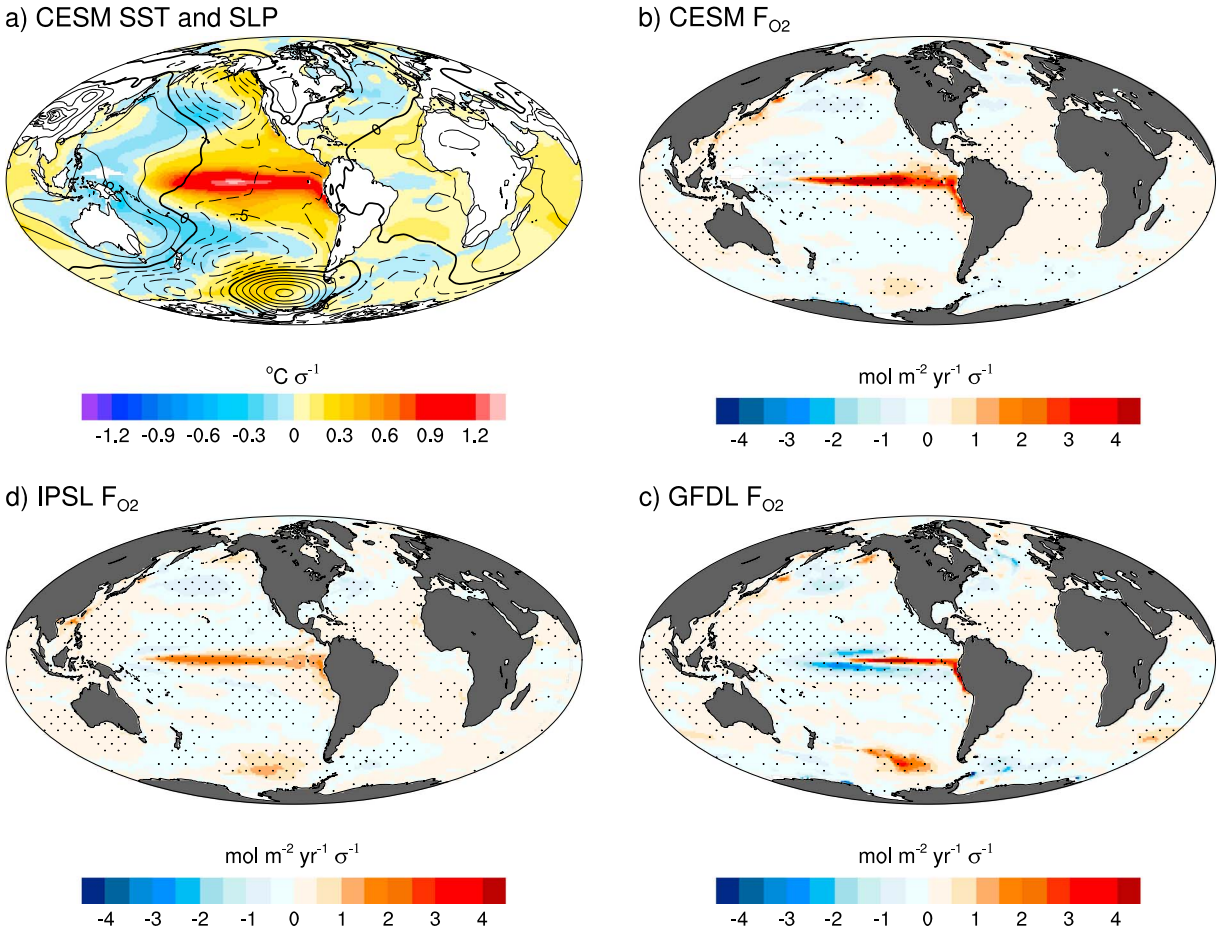

Figure 7. Zero-lag regression of Niño 3.4 index versus anomalies in (a) sea surface temperature (SST; shading) and sea level pressure (SLP; contours) and O_2 fluxes from (b) CESM, (c) IPSL, and (d) GFDL. The dashed contours indicate negative SLP anomalies, contoured every 0.25 hPa. No smoothing was performed on time series prior to regression here to highlight spatial character of anomalies at the peak of ENSO. Stippling indicates 95% significance. Positive flux denotes sea-to-air flux or "outgassing."

hand, the central equatorial Pacific (130°W–180°W) exhibits significant weakening of the easterlies during El Niño (Figure 8e) and is thus sensitive to the localized effects of winds on upwelling rates. The central equatorial Pacific anomaly also likely contains small contributions from the eastward propagation of warm pool waters [*Radenac et al.*, 2005], since these waters were not exposed to intense upwelling and are well equilibrated with the atmosphere. The simulated surface ΔO_2 response is in general agreement with the observed surface O_2 supersaturation reported by *Stephens* [1999] along 120°W–140°W during the El Niño of 1997–1998, suggesting the elimination during this event of the typically high O_2 undersaturation observed along the equator [*Wanninkhof et al.*, 1995].

F_{NCP} acts to offset the total F_{O2} response to ENSO by -14 Tmol yr^{-1} σ^{-1} (0-lag) over the tropical Pacific region (Figure 5b). ENSO-related variability in F_{NCP} in CESM is localized along the eastern tropical Pacific coast and along the equator thru 160°E (Figure 8c). The spatial pattern in the F_{NCP} anomalies is accompanied by simulated changes in surface chlorophyll concentration (Figure 8g), consistent with the fact that variability in photosynthesis rather than respiration drives changes in the net biological production of O_2 in the euphotic zone. Observations show similar impacts of ENSO on primary productivity [*Chavez et al.*, 1999; *Behrenfeld et al.*, 2006], driven by region-specific changes in nutrient supply and light availability. In the eastern equatorial Pacific, changes in net primary productivity are especially sensitive to the effects of Kelvin waves on the depth of the nutricline [*Chavez et al.*, 1999]. In the central Pacific, reduced solar radiation due to enhanced atmospheric convection and the eastward migration of the nutrient-deficient warm pool may also weaken biological productivity in this region [*Park et al.*, 2011; *Feely et al.*, 2002].

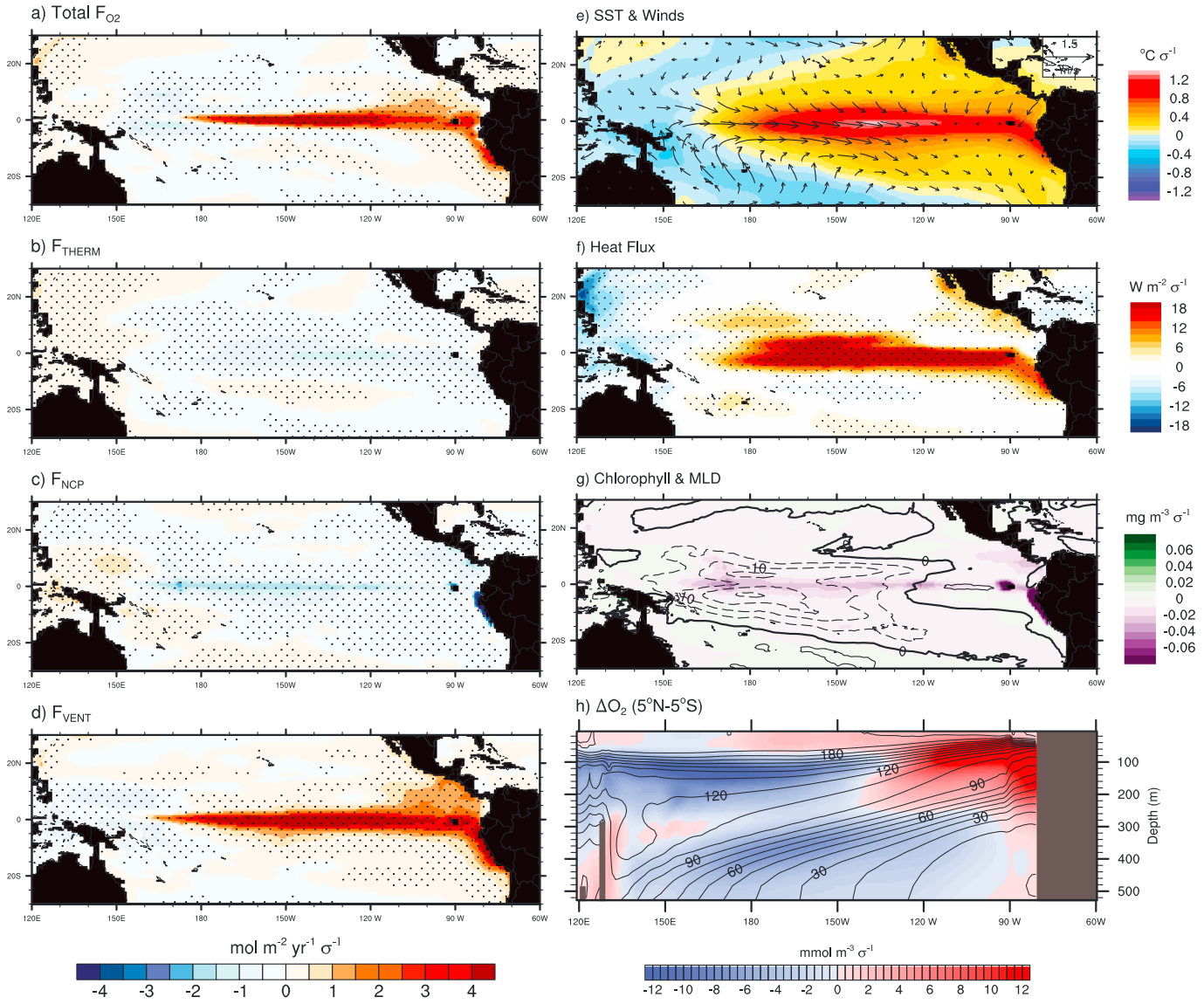

Figure 8. Zero-lag regression of standardized Niño3.4 index versus anomalies in (a) O_2 flux and its components: (b) thermal flux F_{THERM}, (c) net biological production flux F_{NCP}, and (d) ventilation flux term F_{VENT}, alongside (e) SST (shading) and winds (arrows), (f) heat flux, (g) surface chlorophyll concentration (shading) and mixed layer depth (MLD) in contours, and (h) O_2 supersaturation calculated as $\Delta O_2 = [O_2] - [O_2]_{sat}$, superimposed on contours of climatological mean $[O_2]$ (mmol m^{-3}), shown in depth versus longitude, averaged over the 5°N–5°S band. The dashed contours indicate negative MLD anomalies, contoured every 5 m. No smoothing was performed on time series prior to regression here to highlight spatial character of anomalies at the peak of ENSO. Positive flux denotes anomalous sea-to-air flux or "outgassing." Stippling indicates 95% significance.

F_{THERM} contributes only weakly to the F_{O2} response over the tropical Pacific in CESM, damping the total F_{O2} magnitude by -6 Tmol yr^{-1} σ^{-1} (3 month F_{THERM} lag). The sign of its response is nevertheless intriguing. Given the surface warming of the tropical Pacific during El Niño, reduced surface O_2 solubility might be expected to drive thermal outgassing of O_2 [*Rödenbeck et al.*, 2008; *Tohjima et al.*, 2015]. F_{THERM}, however, exhibits a broad anomalous uptake of O_2 during El Niño (Figure 8b). This counterintuitive response arises from the fact that during El Niño, even though tropical Pacific SSTs are warmer, positive heat flux anomalies act to cool the upper ocean (Figure 8f [*Wang and McPhaden*, 2001; *Roemmich and Gilson*, 2011]). Since thermally driven gas exchange scales with heat fluxes rather than SSTs [*Keeling et al.*, 1993], reduced equatorial heat uptake leads to thermal O_2 flux into the ocean during El Niño.

In the western equatorial Pacific, the response of F_{O2} to ENSO is weaker and of opposite sign to that of the eastern and central Pacific (Figure 8a). The shoaling of the western equatorial Pacific thermocline by the

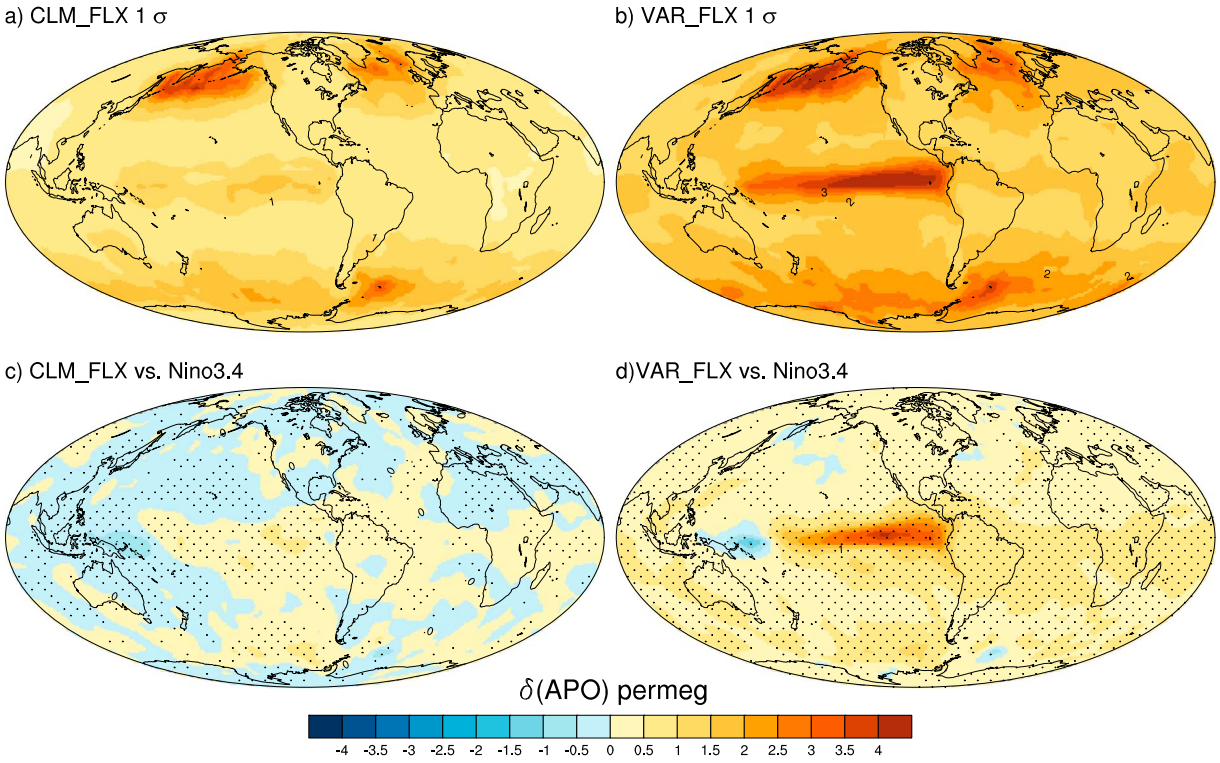

Figure 9. Effects of atmospheric transport on APO variability, shown here as the standard deviation of surface δAPO (per meg) simulated using (a) climatological CESM APO fluxes (CLM_FLX) and (b) variable CESM APO fluxes (VAR_FLX), both transported in TM3. The signature of ENSO is shown as regression of Niño 3.4 index versus anomalies in surface atmospheric δAPO from (c) climatological and (d) variable APO fluxes in per meg σ^{-1}. The stippling indicates 95% significance.

westward propagation of Rossby waves and the eastward migration of the warm pool erodes the fresh "barrier" layer maintained by enhanced precipitation that typically cap upwelling [*Feely et al.*, 2002]. As a result, O_2-poor waters are entrained to the surface, strengthening the ventilation component of the O_2 flux during El Niño, illustrated in Figures 8d and 8g by a negative horseshoe-like F_{VENT} feature and shoaling of mixed layer depth in the western tropical Pacific. Though weak, the opposite response of F_{O2} in this region creates a significant zonal gradient along the equator that is relevant to long-term atmospheric and ocean observations of the western Pacific [e.g., *Tohjima et al.*, 2015].

3.4. APO Modulation by Atmospheric Transport

The influence of ENSO on atmospheric distributions of APO includes contributions from variations in air-sea fluxes as well as changes in atmospheric circulation (e.g., weakening of easterly winds). We isolate the contribution of atmospheric transport by comparing two forward atmospheric transport simulations forced by simulated APO fluxes from CESM and NCEP winds as described in section 2.4: (1) CLM_FLX is an atmospheric transport simulation driven by climatological APO fluxes and interannually varying winds, isolating the effects of atmospheric transport on surface APO anomalies, and (2) VAR_FLX is an atmospheric transport simulation driven by both interannually varying fluxes and winds, containing the effects of both atmospheric transport and air-sea flux variability. The CLM_FLX simulation shows significant APO variability in the North Pacific and North Atlantic but much weaker variance in the middle and low latitudes (Figure 9a). In contrast, VAR_FLX shows widespread APO variability globally, with pronounced variations over regions of high air-sea flux variability such as the eastern and central equatorial Pacific and the Southern Ocean ($\sigma > 4$ per meg; Figure 9b). These atmospheric transport simulations suggest that while atmospheric transport alone can generate APO variability at northern high latitudes, the variability in surface APO at low latitudes and in the Southern Ocean is driven primarily by anomalies in air-sea fluxes.

The imprints of ENSO on atmospheric transport of APO are illustrated in Figure 9c, which shows a regression of APO anomalies from CLM_FLX in the lowest layer of the model against the Niño3.4 index. Figure 9c

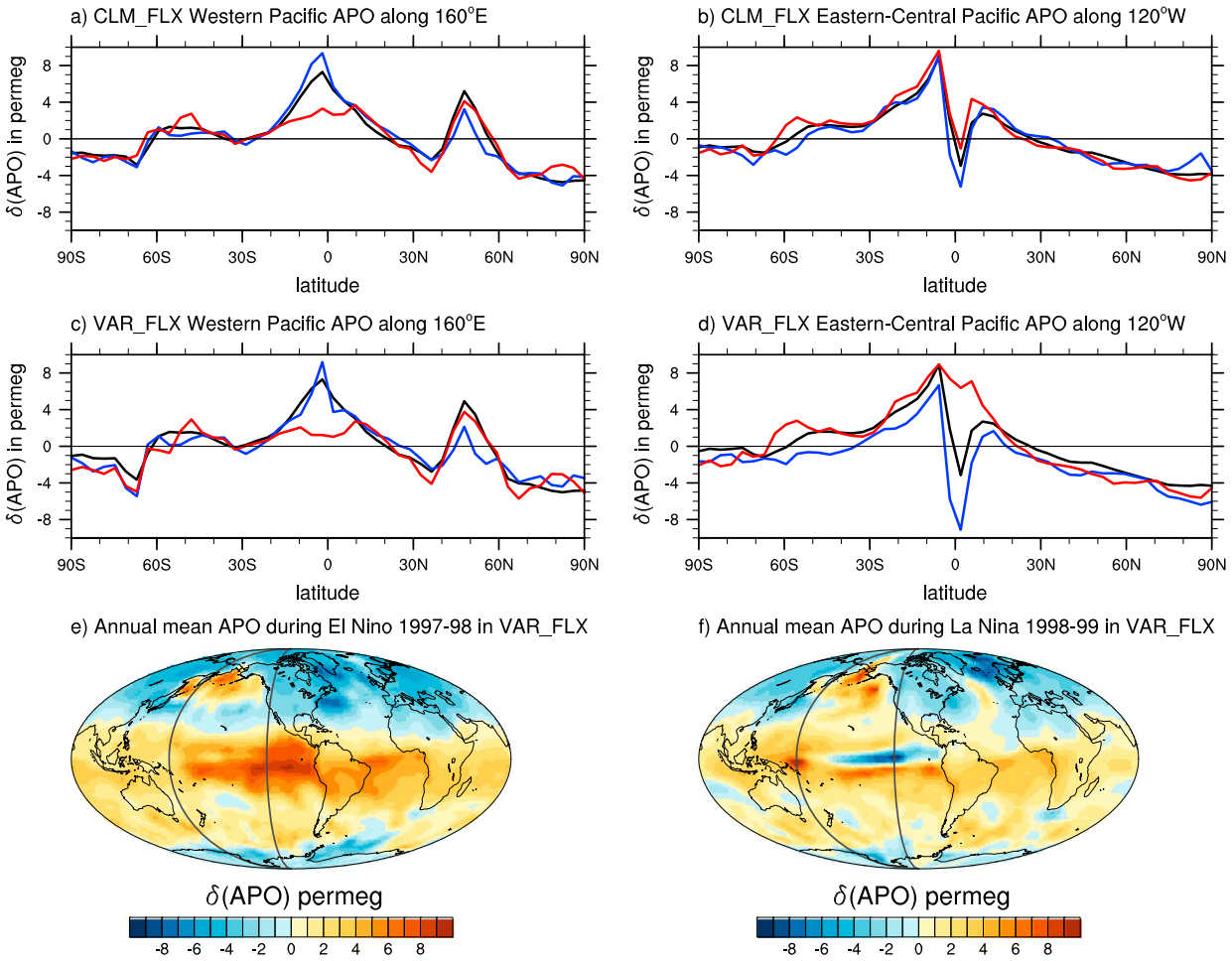

Figure 10. Meridional profile of the annual mean surface APO during the 1997–1998 El Niño (red), the 1998–1999 La Niña (blue), and the long-term mean (black) along (left) 160°E and (right) 120°W for (top) CLM_FLX and (middle) VAR_FLX simulations. (bottom) Annual mean APO from the VAR_FLX simulation for (e) the 97–98 El Niño year and (f) 98–99 La Niña year, calculated from July thru June. The black lines in maps indicate 160°E and 120°W.

shows reduced APO in the western equatorial Pacific countered by a small increase in the eastern equatorial Pacific during El Niño. This effect is likely driven by weakened easterly winds and westerly wind bursts (Figure 8e), causing an eastward shift in the climatological equatorial APO maximum during El Niño. In the VAR_FLX case, however, substantially larger APO increases occur in the eastern and central equatorial Pacific (Figure 9d), driven by ENSO-related anomalies in the air-sea flux of O_2. Figures 9c and 9d suggest that the atmospheric transport effects tend to reinforce the zonal asymmetry driven primarily by the air-sea APO flux response to ENSO, yielding a significant zonal dipole in surface APO distribution during ENSO events.

We illustrate the regional contributions of atmospheric transport and air-sea fluxes in Figure 10, which shows the simulated annual mean surface APO meridional profile along the eastern (120°W) and western (160°E) Pacific during the strong El Niño of 1997–1998 and La Niña of 1998–1999. In both the CLM_FLX and VAR_FLX atmospheric transport simulations (Figures 10a and 10c), the western equatorial Pacific shows a similar increase in APO of about 5 per meg from El Niño to La Niña, suggesting changes in atmospheric transport drive most of the surface APO variability in this region. In the eastern equatorial Pacific, however, there is a substantial decrease of 16 per meg in VAR_FLX from El Niño to La Niña, a value that is not replicated by CLM_FLX, which only shows a 5 per meg decrease. Figure 10 suggests that while ENSO-related changes in atmospheric transport drive most of the surface APO variability in the western tropical Pacific, air-sea flux anomalies dominate the larger surface atmospheric variability of APO found in the eastern and central equatorial Pacific. For reference, the VAR_FLX annual mean APO distribution for

both years are shown in Figures 10e and 10f, emphasizing both the zonal shift in the equatorial APO maximum, as well as a significant change in the global atmospheric APO content due to variability in the equatorial O_2 flux.

4. Summary and Implications

The impacts of ENSO on air-sea O_2 exchange are significant and complex, involving interactions between biogeochemical and physical processes, as illustrated in Figure 11. The atmospheric inversion and ocean model simulations presented here indicate that in an anomalous sense, the upper ocean loses O_2 to the atmosphere during El Niño and gains O_2 during La Niña. In CESM, these anomalies are driven by significant modulation of the O_2 content in the upper equatorial Pacific by coupled ocean-atmosphere dynamics. During El Niño, the deepening of thermocline waters in the eastern equatorial Pacific and the weakening of upwelling lead to significant reductions in the ventilation of O_2-deficient waters, driving anomalous O_2 outgassing. El Niño is also associated with diminished biological productivity and net ocean heat loss, which drives anomalous uptake of O_2. Conversely, during La Niña, intensified upwelling of shoaling thermocline waters strongly reinvigorates the ventilation of low-O_2 waters while weakly enhancing the biological production and thermal outgassing of O_2. The net balance of these effects on the O_2 flux response is dominated by the ventilation effect, so that shallower and weaker upwelling during El Niño leads to anomalous O_2 outgassing, whereas deeper and intensified upwelling during La Niña drives anomalous O_2 uptake. Accounting for most of the APO flux variability, these O_2 flux anomalies are strongly localized along the eastern and central equatorial Pacific and are accompanied by a weaker response of the opposite sign in the western tropical Pacific, driving a zonal gradient in the air-sea O_2 flux response to ENSO.

In the atmosphere, the zonal dipole in surface APO anomalies driven by tropical Pacific F_{O2} is further reinforced by changes in atmospheric wind patterns, reconciling the apparently conflicting APO observations of *Tohjima et al.* [2015] in the western tropical Pacific with the APO inversion of *Rödenbeck et al.* [2008]. In agreement with *Tohjima et al.* [2015], our simulations show that APO variability in the western equatorial Pacific is indeed driven primarily by ENSO-related changes in atmospheric transport. We find, however, that the dominance of this atmospheric transport effect is confined to the western equatorial Pacific and that variations in air-sea fluxes drive the larger surface APO anomalies found in the eastern and central equatorial Pacific.

The magnitude of the APO response in the eastern and central equatorial Pacific is likely model-dependent and is currently poorly sampled. Shipboard measurements of APO in this region [*Battle et al.*, 2006] continued over the past decade may provide improved constraints on the integrated response of the upper ocean O_2 cycle to tropical climate variability. Atmospheric synoptic events, however, can induce substantial variations in this region [*Stephens et al.*, 2003], necessitating long-term observations to filter out short-term variability. Kiritimati Island, Kiribati (2°N, 157°W), located downwind of the epicenter of air-sea O_2 flux variability, is ideally situated for constraining the magnitude of APO variability in the tropical Pacific and its zonal gradient. A new atmospheric O_2 measurement station at Kiritimati Island could thus substantially improve the tropical Pacific sampling capabilities of the Scripps network shown in Figure 3.

Multiple lines of evidence point to significant imprints of ENSO on the spatial distribution of APO and the global APO budget, driven by anomalies in tropical Pacific air-sea O_2 exchange. Our findings are in agreement with results from a hindcast simulation of the MITgcm that shows global impacts of ENSO-related variability in tropical air-sea O_2 fluxes [*McKinley et al.*, 2003]. Based on the extended APO inversion results, variability in APO fluxes of approximately ±34 Tmol yr^{-1} σ^{-1} due to ENSO modulation of air-sea O_2 fluxes should be taken into account in calculating global carbon sink budgets on interannual time scales. This estimate, however, does not take into account the diversity of ENSO phenomena, which may project on the F_{O2} response in the tropical Pacific. The eastern equatorial Pacific region, for instance, is likely to continue taking up O_2 during central Pacific or "Modoki" El Niño events [*Ashok et al.*, 2007]. We also did not address the potential impact of asymmetry between El Niño and La Niña phenomena [*Rodgers et al.*, 2004] on the air-sea O_2 flux response. These potential sensitivities of APO responses to ENSO diversity might be best examined in an extended APO inversion and ocean model simulations that include recent ENSO events, such as the large 2015–2016 El Niño.

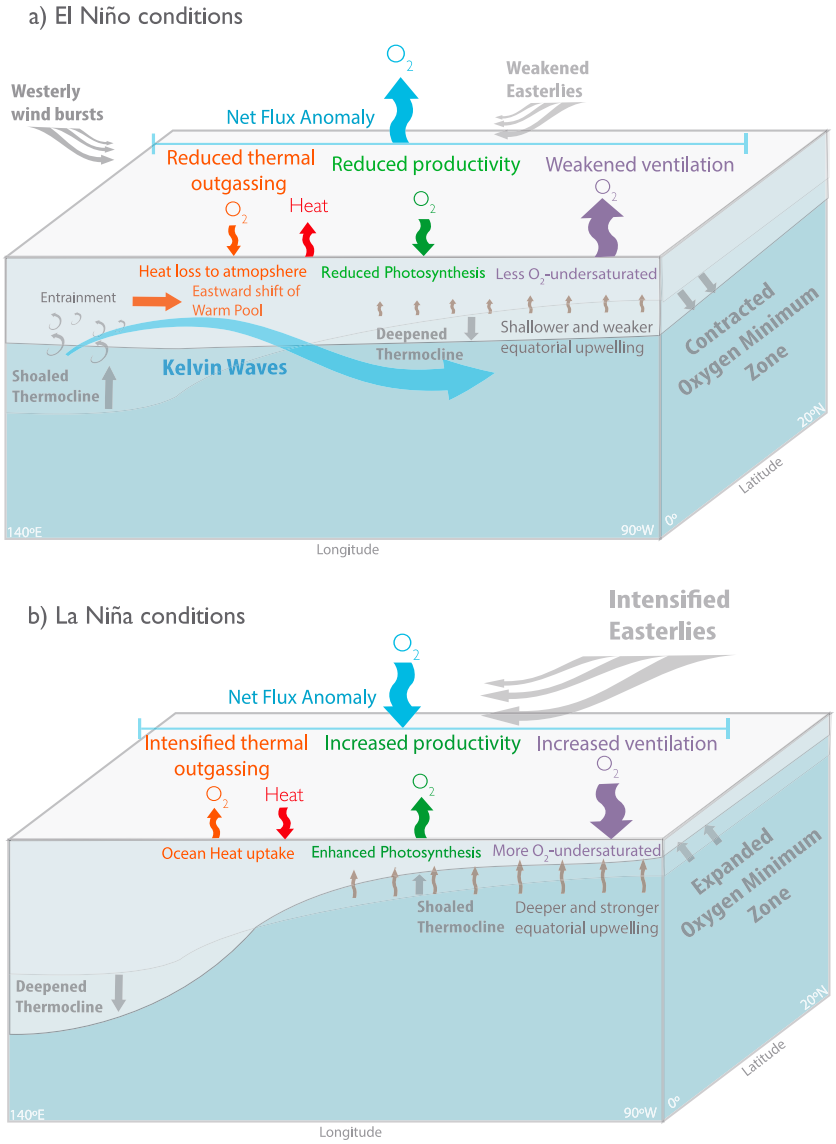

Figure 11. Schematic of anomalies in O_2 fluxes and main driving processes in the tropical Pacific during (a) El Niño and (b) La Niña conditions.

The fidelity of ocean model predictions of future O_2 changes depends on their ability to represent basic aspects of the oceanic O_2 cycle and its natural variability. Both CESM and IPSL show good agreement with the phase and sign of the APO response to ENSO estimated by the atmospheric inversion, whereas the GFDL response showed significant inconsistencies. The magnitude of the APO flux variability, however, is underestimated in all models globally and regionally by more than 50%. This underestimate is in agreement with a previous comparison of the atmospheric inversion APO results to an earlier generation ocean model [*Rödenbeck et al.*, 2008]. A recent study by *Long et al.* [2016] also shows significantly lower interannual variability (>50%) in interior [O_2] in a coupled simulation of CESM when compared to available time series from ocean stations in the Subarctic and Subtropical North Pacific. These underestimations likely result from systemic model deficiencies in representing physical and biogeochemical processes and their interactions. For instance, inadequate representation of Equatorial Intermediate Currents in coarse resolution models [*Dietze and Loeptien*, 2013] or weak vertical mixing in the Subpolar North Pacific (e.g., in CESM [*Moore et al.*, 2013]) leads to weak ventilation of eastern tropical Pacific thermocline waters, driving significant low-O_2 biases. Deficiencies in representing organic matter remineralization profiles may also drive biases in the vertical

gradient of [O_2] in the upper tropical Pacific [*Moore et al.*, 2013], contributing to the large model underestimate in air-sea APO flux variability.

The weak sensitivity of the oceanic O_2 cycle to ENSO in these ocean simulations suggests that climate models may also be underestimating the magnitude of oceanic O_2 loss due to anthropogenic warming. In fact, our reported underestimate of interannual variability is proportionally similar to an underestimate reported by a recent observational analysis of long-term O_2 trends, which shows global oceanic O_2 losses of about 1 Pmol (10^{15} mol) per decade since 1960, exceeding model estimates of 0–600 Tmol per decade [*Schmidtko et al.*, 2017]. An analysis of hydrographic measurements [*Keeling and Garcia*, 2002] also shows a global O_2 outgassing to heating ratio of about 5 nmol (10^{-9}) per Joule (nmol J^{-1}), which are larger than our model estimates of about 3 nmol J^{-1}. These underestimations highlight the need for improved process understanding of subsurface O_2 cycling and circulation on various spatial and time scales.

Still, the simulated O_2 flux response to ENSO provides useful information on the coupling of the oceanic O_2 cycle to climate perturbations in the tropical Pacific. Recent studies suggest the walker circulation may weaken due to anthropogenic warming [*Vecchi and Soden*, 2007]. This may potentially shift the mean state of the tropical Pacific toward El Niño conditions [*Yeh et al.*, 2009], though major uncertainties remain [*Stevenson et al.*, 2012]. Our results indicate a significant and regionally complex response of the upper ocean O_2 budget to El Niño conditions, whereby weakened ventilation leads to oceanic O_2 loss to the atmosphere. The relation between O_2 flux anomalies and changes in interior O_2 distribution and budgets, however, is not clear and merits further investigation. Recent model studies invoke changes in O_2 consumption rates [*Ito and Deutsch*, 2013], as well as reduced ventilation of the OMZ by the shallow overturning cells and zonal jets [*Duteil et al.*, 2014], to explain subsurface [O_2] changes associated with tropical climate variability. The dominance of these processes on subsurface [O_2] variability is likely to be localized and region-specific, given the zonally complex responses of F_{O2} and ΔO_2 shown herein. This regional complexity motivates a closer examination of the basin-wide impacts of tropical climate variability on interior ocean O_2 and their integrated effects on decadal time scales.

Acknowledgments
This material is based on work supported by the National Science Foundation Graduate Research Fellowship under grant DGE-1144086 for Y.E. The authors would also like to acknowledge high-performance computing support from Yellowstone (ark:/85065/d7wd3xhc) provided by NCAR's Computational and Information Systems Laboratory. NCAR is supported by the National Science Foundation. The authors are grateful to Britt Stephens, Jeff Severinghaus, and Shang-Ping Xie for valuable discussions and two anonymous reviewers for their thoughtful reviews. The authors are also sincerely grateful for the efforts of Scripps Atmospheric O_2 Research Program staff, including Sara Ashfar, Adam Cox, and Bill Paplawski. APO data may be obtained by accessing the Scripps Atmospheric Oxygen Research Program website data repository at http://scrippso2.ucsd.edu/data. The air-sea APO flux estimates from the atmospheric inversion are archived in the Jena inversion website: http://www.bgc-jena.mpg.de/~christian.roedenbeck/. The CESM source code is freely available at http://www2.cesm.ucar.edu. The model outputs described in this paper can be accessed at www.earthsystemgrid.org.

References

Alexander, M., I. Blade, M. Newman, J. Lanzante, N. Lau, and J. Scott (2002), The atmospheric bridge: The influence of ENSO teleconnections on air-sea interaction over the global oceans, *J. Clim.*, *15*(16), 2205–2231, doi:10.1175/1520-0442(2002)0152.0.CO;2.

Andrews, O. D., N. L. Bindoff, P. R. Halloran, T. Ilyina, and C. Le Quéré (2013), Detecting an external influence on recent changes in oceanic oxygen using an optimal fingerprinting method, *Biogeosciences*, *10*, 1799–1813, doi:10.5194/bg-10-1799-2013.

Ashok, K., S. K. Behera, S. A. Rao, H. Weng, and T. Yamagata (2007), El Niño Modoki and its possible teleconnection, *J. Geophys. Res.*, *112*, C11007, doi:10.1029/2006JC003798.

Aumont, O., C. Ethé, A. Tagliabue, L. Bopp, and M. Gehlen (2015), PISCES-v2: An ocean biogeochemical model for carbon and ecosystem studies, *Geosci. Model Dev.*, *8*, 2465–2513, doi:10.5194/gmd-8-2465-2015.

Bacastow, R. B. (1976), Modulation of atmospheric carbon dioxide by the southern oscillation, *Nature*, *261*, 116–118, doi:10.1038/261116a0.

Battle, M., et al. (2006), Atmospheric potential oxygen: New observations and their implications for some atmospheric and oceanic models, *Global Biogeochem. Cycles*, *20*, GB1010, doi:10.1029/2005GB002534.

Behrenfeld, M. J., et al. (2006), Climate-driven trends in con-temporary ocean productivity, *Nature*, *444*, 752–755, doi:10.1038/nature05317.

Bjerknes, J. (1969), Atmospheric teleconnections from the equatorial Pacific, *Mon. Weather Rev.*, *97*, 163–172, doi:10.1175/1520-0493(1969)097.

Bopp, L., C. Le Quéré, M. Heimann, A. C. Manning, and P. Monfray (2002), Climate-induced oceanic oxygen fluxes: Implications for the contemporary carbon budget, *Global Biogeochem. Cycles*, *16*(2), 1022, doi:10.1029/2001GB001445.

Bopp, L., et al. (2013), Multiple stressors of ocean ecosystems in the 21st century: Projections with CMIP5 models, *Biogeosciences*, *10*, 6225–6245, doi:10.5194/bg-10-6225-2013.

Bourgeois, T., J. C. Orr, L. Resplandy, C. Ethé, M. Gehlen, and L. Bopp (2016), Coastal-ocean uptake of anthropogenic carbon, *Biogeosciences*, *13*, 4167–4185, doi:10.5194/bg-13-4167-2016.

Brodeau, L., B. Barnier, T. Penduff, A. M. Treguier, and S. Gulev (2009), An ERA40 based atmospheric forcing for global ocean circulation models, *Ocean Model.*, *31*, 88–104, doi:10.1016/j.ocemod.2009.10.005.

Cabré, A., I. Marinov, R. Bernardello, and D. Bianchi (2015), Oxygen minimum zones in the tropical Pacific across CMIP5 models: Mean state differences and climate change trends, *Biogeosciences*, *12*, 5429–5454, doi:10.5194/bg-12-5429-2015.

Chavez, F. P., P. G. Strutton, G. E. Friederich, R. A. Feely, G. C. Feldman, D. G. Foley, and M. J. McPhaden (1999), Biological and chemical response of the equatorial Pacific Ocean to the 1997–98 El Niño, *Science*, *286*, 2126–2131, doi:10.1126/science.286.5447.2126.

Cocco, V., et al. (2013), Oxygen and indicators of stress for marine life in multi-model global warming projections, *Biogeosciences*, *10*, 1849–1868, doi:10.5194/bg-10-1849-2013.

Danabasoglu, G., and J. Marshall (2007), Effects of vertical variations of thickness diffusivity in an ocean general circulation model, *Ocean Model.*, *18*, 122–141, doi:10.1016/j.ocemod.2007.03.006.

Danabasoglu, G., S. Bates, B. P. Briegleb, S. R. Jayne, M. Jochum, W. G. Large, S. Peacock, and S. G. Yeager (2012), The CCSM4 ocean component, *J. Clim.*, *25*, 1361–1389, doi:10.1175/JCLI-D-11-00091.1.

Deser, C., A. S. Phillips, R. A. Tomas, Y. Okumura, M. A. Alexander, A. Capotondi, J. D. Scott, Y.-O. Kwon, and M. Ohba (2012), ENSO and Pacific decadal variability in Community Climate System Model version 4, *J. Clim.*, *25*, 2622–2651, doi:10.1175/JCLI-D-11-00301.1.

Deutsch, C., H. Brix, T. Ito, H. Frenzel, and L. Thompson (2011), Climate-forced variability of ocean hypoxia, *Science*, *333*, 336–339, doi:10.1126/science.1202422.

Dietze, H., and U. Loeptien (2013), Revisiting "nutrient trap- ping" in global coupled biogeochemical circulation models, *Global Biogeochem. Cycles*, *27*, 265–284, doi:10.1002/gbc.20029.

Dietze, H., and A. Oschlies (2005), On the correlation between air-sea heat flux and abiotically induced oxygen gas exchange in a circulation model of the North Atlantic, *J. Geophys. Res.*, *110*, C09016, doi:10.1029/2004JC002453.

Doney, S. C., I. Lima, R. Feely, D. Glover, K. Lindsay, N. Mahowald, J. Moore, and R. Wanninkhof (2009), Mechanisms governing interannual variability in upper-ocean inorganic carbon system and air-sea CO2 fluxes: Physical climate and atmospheric dust, *Deep Sea Res., II*, *56*, 640–655, doi:10.1016/j.dsr2.2008.12.006.

Duchon, C. E. (1979), Lanczos filtering in one and two dimensions, *J. Appl. Meteorol.*, *18*, 1016–1022, doi:10.1175/1520-0450(1979)018.

Dunne, J. P., A. Gnanadesikan, J. L. Sarmiento, and R. D. Slater (2010), Technical description of the prototype version (v0) of Tracers of Phytoplankton with Allometric Zooplankton (TOPAZ) ocean biogeochemical model as used in the Princeton IFMIP model, *Biogeosciences*, *7*, 1–22, doi:10.4195/bg-7-3593-2010.

Duteil, O., C. W. Böning, and A. Oschlies (2014), Variability in subtropical-tropical cells drives oxygen levels in the tropical Pacific Ocean, *Geophys. Res. Lett.*, *41*, 8926–8934, doi:10.1002/2014GL061774.

Ebisuzaki, W. (1997), A method to estimate the statistical significance of a correlation when the data are serially correlated, *J. Clim.*, *10*, 2147–2153, doi:10.1175/1520-0442(1997)010.

Emerson, S., Y. W. Watanabe, T. Ono, and S. Mecking (2004), Temporal trends in apparent oxygen utilization in the upper pycnocline of the North Pacific: 1980–2000, *J. Oceanogr.*, *60*, 139–147, doi:10.1023/B:JOCE.0000038323.62130.a0.

Feely, R. A., R. Wanninkhof, T. Takahashi, and P. Tans (1999), Influence of El Niño on the equatorial Pacific contribution to atmospheric CO_2 accumulation, *Nature*, *398*, 597–601, doi:10.1038/19273.

Feely, R. A., et al. (2002), Seasonal and interannual variability of CO_2 in the equatorial Pacific, *Deep Sea Res., II Top. Stud. Oceanogr.*, *49*, 2443–2469, doi:10.1016/S0967-0645(02)00044-9.

Frölicher, T. L., F. Joos, G. K. Plattner, M. Steinacher, and S. C. Doney (2009), Natural variability and anthropogenic trends in oceanic oxygen in a coupled carbon cycle-climate model ensemble, *Global Biogeochem. Cycles*, *23*, GB1003, doi:10.1029/2008GB003316.

Garcia, H. E., and L. I. Gordon (1992), Oxygen solubility in seawater: Better fitting equations, *Limnol. Oceanogr.*, *37*, 1307–1312, doi:10.4319/lo.1992.37.6.1307.

Garcia, H. E., R. A. Locarnini, T. P. Boyer, J. I. Antonov, A. V. Mishonov, O. K. Baranova, M. M. Zweng, J. R. Reagan, and D. R. Johnson (2014), World Ocean Atlas 2013, in *Volume 3: Dissolved Oxygen, Apparent Oxygen Utilization, and Oxygen Saturation*, edited by S. Levitus and A. Mishonov, pp. 1–19, NOAA Atlas NESDIS 75, Silver Spring, Md.

Gent, P. R., and J. McWilliams (1990), Isopycnal mixing in ocean circulation models, *J. Phys. Oceanogr.*, *20*, 150–155, doi:10.1175/1520-0485(1990)020.

Gent, P. R., et al. (2011), The Community Climate System Model version 4, *J. Clim.*, *24*, 4973–4991, doi:10.1175/2011JCLI4083.1.

Griffies, S., et al. (2009), Coordinated Ocean-Ice Reference Experiments (COREs), *Ocean Model.*, *26*, 1–46, doi:10.1016/j.ocemod.2008.08.007.

Griffies, S. M., M. Winton, B. Samuels, G. Danabasoglu, S. Yeager, S. Marsland, and H. Drange, M. Bentsen (2012), Datasets and protocol for the CLIVAR WGOMD Coordinated Ocean sea-ice Reference Experiments (COREs). WCRP, Report No. 21/2012.

Gruber, N., E. Gloor, S. M. Fan, and J. L. Sarmiento (2001), Air-sea flux of oxygen estimated from bulk data: Implications for the marine and atmospheric oxygen cycles, *Global Biogeochem. Cycles*, *15*, 783–803, doi:10.1029/2000GB001302.

Hamme, R. C., and S. R. Emerson (2004), The solubility of neon, nitrogen and argon in distilled water and seawater, *Deep Sea Res., I*, *51*, 1517–1528, doi:10.1016/j.dsr.2004.06.009.

Hamme, R., and R. F. Keeling (2008), Ocean ventilation as a driver of interannual variability in atmospheric potential oxygen, *Tellus*, *60B*, doi:10.1111/j.1600-0889.2008.00376.x.

Heimann, M. and S. Korner (2003), The global atmospheric tracer model TM3, *Tech. Rep. 5*, Max Planck Inst. for Biogeochem., Jena, Germany.

Helm, K. P., N. L. Bindoff, and J. A. Church (2011), Observed decreases in oxygen content of the global ocean, *Geophys. Res. Lett.*, *38*, L23602, doi:10.1029/2011GL049513.

Hunke, E., and W. Lipscomb (2008), CICE: The Los Alamos sea ice model documentation and software user's manual, version 4.0, *Los Alamos Natl. Lab. Tech. Rep. LA-CC-06-012*, 76 pp.

Ito, T., and C. Deutsch (2010), A conceptual model for the temporal spectrum of oceanic oxygen variability, *Geophys. Res. Lett.*, *37*, L03601, doi:10.1029/2009GL041595.

Ito, T., and C. Deutsch (2013), Variability of the oxygen minimum zone in the tropical North Pacific during the late twentieth century, *Global Biogeochem. Cycles*, *27*, 1119–1128, doi:10.1002/2013GB004567.

Jin, X., R. G. Najjar, F. Louanchi, and S. C. Doney (2007), A modeling study of the seasonal oxygen budget of the global ocean, *J. Geophys. Res.*, *112*, C05017, doi:10.1029/2006JC003731.

Kalnay, E., et al. (1996), The NCEP/NCAR 40-Year Re-analysis Project, *Bull. Am. Meteorol. Soc*, *77*, 437–471, doi:10.1175/1520-0477(1996)077.

Keeling, C. D., and R. Revelle (1985), Effects of El-Niño Southern Oscillation on the atmospheric content of carbon-dioxide, *Meteoritics*, *20*, 437–450.

Keeling, R., and A. Manning (2014), Studies of recent changes in atmospheric O_2 content, *Treatise on Geochemistry*, 2nd ed., edited by H. D. Holland and K. K. Turekian, pp. 385–404, Elsevier, Amsterdam, Netherlands, doi:10.1016/B978-0-08-095975-7.00420-4.

Keeling, R. F., and H. Garcia (2002), The change in oceanic O_2 inventory associated with recent global warming, *Proc. Natl. Acad. Sci. U.S.A.*, *99*, 7848–7853, doi:10.1073/pnas.122154899.

Keeling, R. F. and J. P. Severinghaus (2000), Atmospheric oxygen and the carbon cycle, in *The Carbon Cycle*, edited by T. M. L. Wigley and D. S. Schimel, pp. 134–140, Cambridge Univ. Press, Boston, Mass.

Keeling, R. F., R. P. Najjar, M. L. Bender, and P. P. Tans (1993), What atmospheric oxygen measurements can tell us about the global carbon cycle, *Global Biogeochem. Cycles*, *7*, 37–67, doi:10.1029/92GB02733.

Keeling, R. F., S. C. Piper, and M. Heimann (1996), Global and hemispheric CO_2 sinks deduced from changes in atmospheric O_2 concentration, *Nature*, *381*, 218–221, doi:10.1038/381218a0.

Keeling, R. F., B. B. Stephens, R. G. Najjar, S. C. Doney, D. Archer, and M. Heimann (1998), Seasonal variations in the atmospheric O2/N2 ratio in relation to the kinetics of air-sea gas exchange, *Global Biogeochem. Cycles*, *12*(1), 141–163, doi:10.1029/97GB02339.

Keeling, R. F., A. Körtzinger, and N. Gruber (2010), Ocean deoxygenation in a warming world, *Annu. Rev. Mater. Sci.*, *2*, 199–229, doi:10.1146/annurev.marine.010908.163855.
Large, W. G., and S. Yeager (2009), The global climatology of an interannually varying air-sea flux data set, *Clim. Dyn.*, *33*, 341–364, doi:10.1007/s00382-008-0441-3.
Large, W. G., J. C. McWilliams, and S. C. Doney (1994), Oceanic vertical mixing: A review and a model with a nonlocal boundary layer parameterization, *Rev. Geophys.*, *32*, 363–403, doi:10.1029/94RG01872.
Long, M. C., K. Lindsay, S. Peacock, J. K. Moore, and S. C. Doney (2013), Twentieth-century oceanic carbon uptake and storage in CESM1 (BGC), *J. Clim.*, *26*, 6775–6800, doi:10.1175/JCLI-D-12-00184.1.
Long, M. C., C. A. Deutsch, and T. Ito (2016), Finding forced trends in oceanic oxygen, *Global Biogeochem. Cycles*, *30*, 381–397, doi:10.1002/2015GB005310.
Madec, G. (2008) *NEMO Ocean Engine. Note du Pole de modélisation de l'Institut Pierre-Simon Laplace*, vol. 27, pp. 1–217, Institut Pierre-Simon Laplace (IPSL), France.
Manning, A. C. (2001), Temporal variability of atmospheric oxygen from both continuous measurements and a flask sampling network: Tools for studying the global carbon cycle, PhD thesis, Univ. of California, La Jolla, Calif.
Manning, A. C., and R. F. Keeling (2006), Global oceanic and land biotic carbon sinks from the Scripps atmospheric oxygen flask sampling network, *Tellus, Ser. B*, *58*, 95–116, doi:10.1111/j.1600-0889.2006.00175.x.
McKinley, G. A., M. J. Follows, J. Marshall, and S. M. Fan (2003), Interannual variability of air-sea O_2 fluxes and the determination of CO_2 sinks using atmospheric O_2/N_2, *Geophys. Res. Lett.*, *30*(3), 1101, doi:10.1029/2002GL016044.
McKinley, G. A., M. J. Follows, and J. Marshall (2004), Mechanisms of air-sea CO_2 flux variability in the equatorial Pacific and the North Atlantic, *Global Biogeochem. Cycles*, *18*, GB2011, doi:10.1029/2003GB002179.
McPhaden, M. J., et al. (1998), The tropical ocean-global atmosphere observing system: A decade of progress, *J. Geophys. Res.*, *103*, 14,169–14,240, doi:10.1029/97JC02906.
Moore, J. K., S. C. Doney, and K. Lindsay (2004), Upper ocean ecosystem dynamics and iron cycling in a global three-dimensional model, *Global Biogeochem. Cycles*, *18*, GB4028, doi:10.1029/2004GB002220.
Moore, J. K., K. Lindsay, S. C. Doney, M. C. Long, and K. Misumi (2013), Marine ecosystem dynamics and biogeochemical cycling in the Community Earth System Model [CESM1(BGC)]: Comparison of the 1990s with the 2090s under the RCP 4.5 and RCP 8.5 scenarios, *J. Clim.*, *26*, 9291–9312, doi:10.1175/jcli-d-12-00566.1.
Najjar, R. G., and R. F. Keeling (2000), Mean annual cycle of the air- sea oxygen flux: A global view, *Global Biogeochem. Cycles*, *14*, 573–584, doi:10.1029/1999GB900086.
Nevison, C., et al. (2015), Evaluating the ocean biogeochemical components of Earth system models using atmospheric potential oxygen and ocean color data, *Biogeosciences*, *12*, 193–208, doi:10.5194/bg-12-193-2015.
Park, J. Y., J. S. Kug, J. Park, S. W. Yeh, and C. J. Jang (2011), Variability of chlorophyll associated with El Niño–Southern Oscillation and its possible biological feedback in the equatorial Pacific, *J. Geophys. Res.*, *116*, C10001, doi:10.1029/2011JC007056.
Radenac, H., Y. Dandonneau, and B. Blanke (2005), Displacements and transformations of nitrate-rich and nitrate-poor water masses in the tropical Pacific during the 1997 El Niño, *Ocean Dyn.*, *55*, 34–46, doi:10.1007/s10236-005-0111-5.
Resplandy, L., R. Séférian, and L. Bopp (2014), Natural variability of CO_2 and O_2 fluxes: What can we learn from centuries-long climate models simulations?, *J. Geophys. Res. Oceans*, *120*, 384–404, doi:10.1002/2014JC010463.
Rödenbeck, C., C. LeQuéré, M. Heimann, and R. F. Keeling (2008), Interannual variability in oceanic biogeochemical processes inferred by inversion of atmospheric O_2/N_2 and CO_2 data, *Tellus B*, *60*, 685–705, doi:10.1111/j.1600-0889.2008.00375.x.
Rodgers, K. B., P. Friederichs, and M. Latif (2004), Tropical Pacific decadal variability and its relation to decadal modulations of ENSO, *J. Clim.*, *17*, 3761–3774, doi:10.1175/1520-0442(2004)017.
Rodgers, K. B., et al. (2009), Using altimetry to help explain patchy changes in hydrographic carbon measurements, *J. Geophys. Res.*, *114*, C09013, doi:10.1029/2008JC005183.
Rodgers, K. B., J. Lin, and T. L. Frölicher (2015), Emergence of multiple ocean ecosystem drivers in a large ensemble suite with an earth system model, *Biogeosciences*, *12*(11), 3301–3320, doi:10.5194/bg-12-3301-2015.
Roemmich, D., and J. Gilson (2011), The global ocean imprint of ENSO, *Geophys. Res. Lett.*, *38*, L13606, doi:10.1029/2011GL047992.
Sarmiento, J. L., T. C. Hughes, R. J. Stouffer, and S. Manabe (1998), Simulated response of the ocean carbon cycle to anthropogenic climate warming, *Nature*, *393*, 245–249, doi:10.1038/30455.
Schmidtko, S., L. Stramma, and M. Visbeck (2017), Decline in global oceanic oxygen content during the past five decades, *Nature*, *542*, 335–339, doi:10.1038/nature21399.
Severinghaus, J. P. (1995), Studies of the terrestrial O_2 and carbon cycles in sand dune gases and in biosphere 2, PhD thesis, Columbia Univ., New York.
Smith, R. D., et al. (2010), The Parallel Ocean Program (POP) reference manual, *Los Alamos Natl. Lab. Tech. Rep. LAUR-10-01853*, 140 pp.
Stephens, B. B. (1999), Field-based atmospheric oxygen measurements and the ocean carbon cycle, PhD. Thesis, Univ. of California, San Diego, Calif.
Stephens, B. B., R. F. Keeling, M. Heimann, K. D. Six, R. Murnane, and K. Caldeira (1998), Testing global ocean carbon cycle models using measurements of atmospheric O_2 and CO_2 concentration, *Global Biogeochem. Cycles*, *12*, 213–230, doi:10.1029/97GB03500.
Stephens, B. B., R. F. Keeling, and W. Paplawsky (2003), Shipboard measurements of atmospheric oxygen using a vacuum-ultraviolet absorption technique, *Tellus*, *55B*, 857–878, doi:10.3402/tellusb.v55i4.16386.
Stevenson, S., B. Fox-Kemper, M. Jochum, R. Neale, C. Deser, and G. Meehl (2012), Will there be a significant change to El Niño in the twenty-first century?, *J. Clim.*, *25*, 2129–2145, doi:10.1175/JCLI-D-11-00252.1.
Stramma, L., G. C. Johnson, J. Sprintall, and V. Mohrholz (2008), Expanding oxygen-minimum zones in the tropical oceans, *Science*, *320*, 655–658, doi:10.1126/science.1153847.
Stramma, L., A. Oschlies, and S. Schmidtko (2012), Mismatch between observed and modeled trends in dissolved upper-ocean oxygen over the last 50 yr, *Biogeosciences*, *9*, 4045–4057, doi:10.5194/bg-9-4045-2012.
Takahashi, T., R. Feely, R. Weiss, R. Wanninkhof, D. Chipman, S. Sutherland, and T. Takahashi (1997), Global air-sea flux of CO_2: An estimate based on measurements of sea-air pCO_2 difference, *Proc. Natl. Acad. Sci. U.S.A.*, *94*, 8292–8299.
Tohjima, Y., Y. Terao, H. Mukai, T. Machida, Y. Nojiri, and S. Maksyutov (2015), ENSO-related variability in latitudinal distribution of annual mean atmospheric potential oxygen (APO) in the equatorial western Pacific, *Tellus B.*, *67*, 25,869, doi:10.3402/tellusb.v67.25869.
Trenberth, K. E. (1997), The definition of El Niño, *Bull. Am. Meteorol. Soc.*, *78*, 2771–2777, doi:10.1175/1520-0477(1997)078.
Trenberth, K. E., J. M. Caron, D. P. Stepaniak, and S. Worley (2002), The evolution of ENSO and global atmospheric surface temperatures, *J. Geophys. Res.*, *107*(D8), AAC 5-1–AAC 5-17, doi:10.1029/2000JD000298.

Vecchi, G. A., and B. J. Soden (2007), Global warming and the weakening of the tropical circulation, *J. Clim.*, *20*, 4316–4340, doi:10.1175/JCLI4258.1.JCLI3631.1.

Wang, W., and M. J. McPhaden (2001), Surface layer heat balance in the equatorial Pacific Ocean during the 1997–98 El Niño and the 1998–99 La Niña, *J. Clim.*, *14*, 3393–3407, doi:10.1175/1520-0442(2001)014.

Wanninkhof, R. (1992), Relationship between wind speed and gas exchange over the ocean, *J. Geophys. Res.*, *97*(C5), 7373–7382, doi:10.1029/92JC00188.

Wanninkhof, R., R. A. Feely, D. K. Atwood, G. A. Berberian, W. D. Wilson, P. P. Murphy, and M. F. Lamb (1995), Seasonal and lateral variations in carbon chemistry of surface water in the eastern equatorial Pacific during 1992, *Deep Sea Res., Part II*, *42*(2–3), 387–410, doi:10.1016/0967-0645(95)00016-J.

Weiss, R. F. (1974), Carbon dioxide in seawater: The solubility of an ideal gas, *Mar. Chem.*, *2*, 203–215, doi:10.1016/0304-4203(74)90015-2.

Williams, R. G., and M. J. Follows (2011), *Ocean Dynamics and the Carbon Cycle*, pp. 150–151, Cambridge Univ. Press, Cambridge, U. K.

Winguth, A. M. E., M. Heimann, K. D. Kurz, E. Maier-Reimer, U. Milolajewicz, and J. Segschneider (1994), El Niño Southern Oscillation related fluctuations in the marine carbon cycle, *Global Biogeochem. Cycles*, *8*(1), 39–93, doi:10.1029/93GB03134.

Yeh, S. W., J. S. Kug, B. Dewitte, M. H. Kwon, B. P. Kirtman, and F. F. Jin (2009), El Niño in a changing climate, *Nature*, *461*, 511–514, doi:10.1038/nature08316.

Zwiers, F. W., and H. von Storch (1995), Taking serial correlation into account in tests of the mean, *J. Clim.*, *8*, 336–351, doi:10.1175/1520-0442(1995)008.